Self-archived version of the article published in International Journal of Heat and Mass Transfer:
N. Cancilla, L. Gurreri, G. Marotta, M. Ciofalo, A. Cipollina, A. Tamburini, G. Micale
CFD prediction of shell-side flow and mass transfer in regular fiber arrays,
International Journal of Heat and Mass Transfer, 168, 2021, 120855.
https://doi.org/10.1016/j.ijheatmasstransfer.2020.120855

CFD prediction of shell-side flow and mass transfer in regular fiber arrays

N. Cancilla[a], L. Gurreri[a*], G. Marotta[b], M. Ciofalo[a], A. Cipollina[a], A. Tamburini[a], G. Micale[a]

[a]*Dipartimento di Ingegneria, Università degli Studi di Palermo, viale delle Scienze ed. 6, 90128 Palermo, Italy*

[b]*Medtronic, via Camurana 1, 41037, Mirandola, Modena, Italy*

[*]corresponding author – email: luigi.gurreri@unipa.it

Abstract

This paper reports high-accuracy numerical simulations of fully developed flow with mass transfer in fiber bundles arranged in regular square or hexagonal lattices under steady-state conditions. The porosity ε was kept fixed at 0.5 and the Schmidt number at ~500 (representative of urea transport in hollow-fiber haemodialysis units), while a large number of combinations of axial flow, transverse flow and flow attack angles in the cross-section plane were considered. In particular, both the axial and the transverse Reynolds numbers Re_z, Re_T were made to vary from 10^{-4} to 10^{2}. Where possible, results were compared with the literature in terms of hydraulic permeability or Kozeny constant. The issue of concentration boundary conditions, and the appropriate definition of an average Sherwood number, were specifically addressed. Both the hexagonal and the square lattice were found to be hydraulically almost isotropic up to transverse flow Reynolds numbers Re_T of ~10, while they behaved anisotropically in regard to mass transfer even at Re_T as low as 0.1. As expected, a larger anisotropy was exhibited by the square lattice. In mixed (axial+transverse) flow condition, the transverse friction coefficient was almost completely unaffected by the simultaneous presence of an axial flow, while the axial friction coefficient (and thus the axial pressure loss) increased with the transverse Reynolds number for Re_T>~5-10. In regard to mass transfer, the Sherwood number settled in all cases to the higher between the Sherwood number in purely transverse flow and that in purely axial flow.

Keywords*: Computational Fluid Dynamics, viscous flow, shell-side mass transfer, rod array, cylinder array.*

1. Introduction

Hollow fiber membrane modules are used in a wide range of separation processes. These devices are mass exchangers due to the porosity of the fibers wall and their design is similar to that of shell and tube heat exchangers. A typical module (**Figure 1**) consists of a cylindrical housing (shell) enclosing a bundle of hollow fibers, which are cylindrically shaped membranes. Fiber ends are embedded in polyurethane plugs to keep the lumen-side and shell-side fluids separated.

These contactors can be used in several industrial processes and biomedical applications, including liquid-liquid extraction and gas absorption (1-3), water desalination by membrane distillation (4) or reverse osmosis (5), water treatment by ultrafiltration (6), air humidification (7) and blood-contacting medical devices for the replacement of human organ functions or for the treatment of diseases, as in haemodialysis (8,9) and blood oxygenators (10).

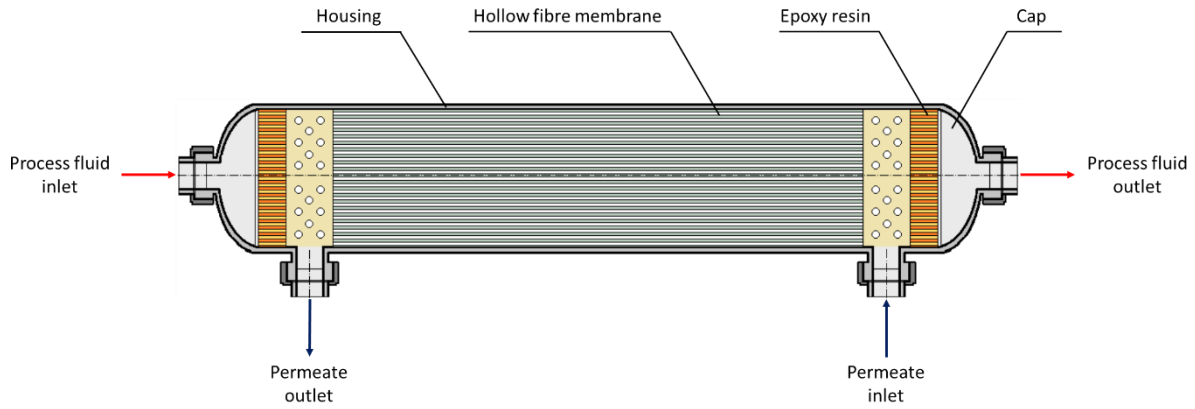

Figure 1: A typical hollow fiber membrane module operating in counter-current contacting mode.

The widespread use of hollow fiber membranes in recent decades is due to their advantages over other module types, in particular the high packing density and high specific surface area. For example, in the case of extraction (11), the main benefits over conventional equipment are higher specific area for mass transfer, no flooding and the possibility of reducing or even avoiding entrainment. In membrane distillation, the use of hollow fibers is interesting due to their high exchange surface area and modular versatility (4). In air humidification, the pressure drop in the air side (shell-side, transverse flow) is suitable for practical applications, while the heat and mass transfer coefficients are still high, with satisfactory humidification efficiencies (7).

In biomedical processes, hollow fiber membrane contactors offer a high selective interaction between two fluids while avoiding any contact between them (8). Also, in ultrafiltration (6) these contactors have the highest area/volume ratio compared to other types of membrane modules and guarantee, especially in haemodialysis, the lowest cost, which is fundamental for all applications requiring

disposable cartridge membrane modules. The moderate pressure drop makes hollow fiber modules very efficient in terms of energy consumption (12).

In the past, the usual approach to predict transport phenomena was the use of engineering correlations for friction and mass transfer (11, 13-14). For the calculation of the overall mass transfer coefficient, the resistances of lumen-side and shell-side boundary layers and of the membrane itself have all to be taken into account. On the lumen side, the fluid flows essentially through tubes in parallel, so that flow and mass transfer can be studied by using analytical solutions (15) and/or empirical correlations (1) for pipe flow available in the literature. The contribution of the membrane depends only on the properties of the membrane itself (permeability, inner diameter and wall thickness). On the other hand, fluid dynamics and associated transport phenomena on the shell-side can be important for the process performance (16), so that their characterization can be crucial for optimization purposes. For example, Mavroudi *et al.* (17) studied gas-liquid processes for carbon dioxide absorption in water, showing that the shell-side resistance was the dominant one (68–78% of the total) at low water flow rates (up to 9.45×10^{-5} m^3/s).

Several authors developed axial laminar flow models to describe mass transfer by assuming uniformly packed fiber bundles (18-21). The effect of packing non-uniformity on flow maldistribution was experimentally characterized by using a tracer (22). Theoretical models based on the Hagen-Poiseuille equation were developed to analyse the flow in the lumen side either with or without fouling near the outlet of a single fiber (23).

The impact of shell-side fluid flow configuration (e.g. parallel-flow or cross-flow) on module performance was also assessed. Wickramasinghe *et al*. (13) demonstrated that the cross-flow arrangement offers higher mass transfer coefficients and lower shell-side pressure drops compared to the parallel flow layout. Zheng *et al.* (24) stated that the non-ideal flow distribution resulting from uneven inter-fiber spacing can be disadvantageous for the performance. Additional studies were performed to clarify the manifolds' influence on shell flow uniformity (7,25).

Computational fluid dynamics (CFD) provides a useful tool to predict flow and mass / heat transport phenomena in fiber bundle devices. Computer simulations allow the flow to be modelled in complex geometries, thus reducing the effort of module design compared to the more expensive and time-consuming experimental approach.

Pak *et al*. (26) used a finite volume method to solve the two-dimensional flow and particle transport equations in laminar flow over the permeable surface of a tubular membrane. The work aimed at studying the effect of various physical parameters on the growth of concentration polarization layer along the membrane surface. Zhuang *et al*. (12, 27) focused on how geometrical parameters affected the mass flux distribution, showing that reducing membrane permeability or pressure drop on both feed and permeate sides could improve the uniformity of flux distribution. A two-dimensional model

describing the hydrodynamic and thermal conditions in a single hollow fiber module under laminar flow conditions was developed by Yu *et al.* (28) for the membrane distillation process. The model, in which the computational domain was made of 2D axial-symmetric single-fiber cylindrical structures, was able to predict the overall performance of the module in terms of fluxes and temperatures. Yang *et al.* (4) evaluated the performance of shell-side feed membrane distillation systems with nine different types of modified fiber geometries via 3D CFD modelling. The module with fibers of gear-shaped structure achieved the highest average performance and mass flux values compared to the original straight design, followed by the alternate wavy fibers. Eloot *et al.* (9) developed a finite volume 3D-model over the complete length of the hollow fiber module for haemodialysis, assuming the fibers to be arranged in a hexagonal lattice. For symmetry reasons, the computational domain was a twelfth part of a single fiber with its surrounding membrane and shell-side compartment. The permeability characteristics of the membrane were calculated from laboratory tests for forward and back-filtration. From the calculated pressure distribution, the impact of flow, haematocrit and capillary dimensions on the presence and localization of back-filtration were investigated. After performing the simulations for different module geometries, the same group found that mass transfer is enhanced for longer or finer fibers (29).

Dierickx *et al.* (30) developed a two-dimensional model for flow and mass transfer in cross-flow hollow fiber membrane artificial lungs by using a finite element technique in a computational domain consisting of a single-fiber cell. Three different fiber bank configurations were studied: in-line square, equilateral triangle and staggered square, with porosity values from 0.4 to 0.6. Günther *et al.* (31) studied how the packing density (at three different values) of the fibers arranged in hexagonal unit cells can affect the performance of the modules in terms of the filtration velocity and, particularly, of the spatial distribution of permeate velocity along the whole fiber length. Based on the previous study, another model was also developed (32) in which each fiber was modelled as a circular cell surrounded by the associated fluid. The model aimed to predict the combined effects of packing density, fiber length, fiber inner diameter and other quantities on local flux distribution and permeate output flow rate.

Zhang *et al.* (33) simulated fluid flow at different Reynolds numbers in a microscale CFD model for artificial lung devices and haemodialysis modules. Square, diagonal, and random 3D fiber arrays with the same porosity were simulated, and the distributions of shear stress were compared. The 3D fiber bundle simulation results showed that three dimensional effects are not negligible, as velocity and shear stress distribution can vary significantly along the fibers' axial direction. Single and multi-phase flows through submerged membrane units with irregular fiber arrangement were investigated by Buetehorn *et al*. (34) by CFD. The computational domains were based on computed tomography

scans mapping the distribution of hollow fibers at different axial locations in a commercial membrane bundle. Results showed an anisotropic resistance to the flow.

Despite the numerous studies dedicated to the subject, a systematic knowledge of the flow and mass transfer characteristics of fiber bundles is still lacking. In particular, the influence of the boundary conditions (e.g. uniform wall mass flux versus uniform wall concentration) and the influence of the flow attack angle are only poorly known, and the case of very low Reynolds numbers (creeping flow), uninteresting as it may look, probably deserves a more close scrutiny.

Therefore, a research project was initiated aimed at studying the shell-side flow and mass transfer characteristics both of regular lattices and of random distributions, representative of hollow fiber membrane bundles subject to parallel-, cross- and mixed-flow configurations. Simulation results at unit cell level will be used to develop 3D models of whole haemodialysis modules, based on a porous media approach as used in several published studies (10,35,36).

The present work deals with regular, square and hexagonal, arrays of fibers. The case of random fiber distributions, and the porous-media simulation of whole modules, will be the subject of further works.

2. Models and methods

2.1 Computational domains

In this work, fluid flow and mass transfer around bundles of straight, axially indefinite, fibers were simulated by Computational Fluid Dynamics in order to evaluate shell-side pressure drop per unit length and shell-side mass transport performance (Sherwood number). The study was conducted at Unit Cell (UC) level (37-38), i.e. the computational domain was a repetitive periodic unit of the bundle including a single fiber.

The porosity ε was defined as:

$$\varepsilon = \frac{V}{V_{tot}} \tag{1}$$

in which V_{tot} is the total volume, including shell and lumen (not simulated), while V is the volume of fluid. In the present study the bundle porosity was kept fixed at 50% and the outer diameter d of the fibers was set to 280 μm; both values are typical of commercial haemodialysis units.

Figure 2 shows the computational domains and the dimensions chosen for a hexagonal lattice (sometimes called equilateral triangular lattice) (a) and a regular square lattice (b).

In all cases, in the axial direction z the cell geometry was assumed to be uniform and the flow and concentration fields fully developed, so that the extent of the computational domain along this direction was irrelevant and was arbitrarily set to 500 μm. The computational grid along the z direction included only three finite volumes, which is the minimum number required by the

mathematical treatment of the problem in the finite volume code Ansys-CFX 18®. Graphs (c) and (d) show the main flow direction T and the flow attack angle θ in the plane of the cross section.

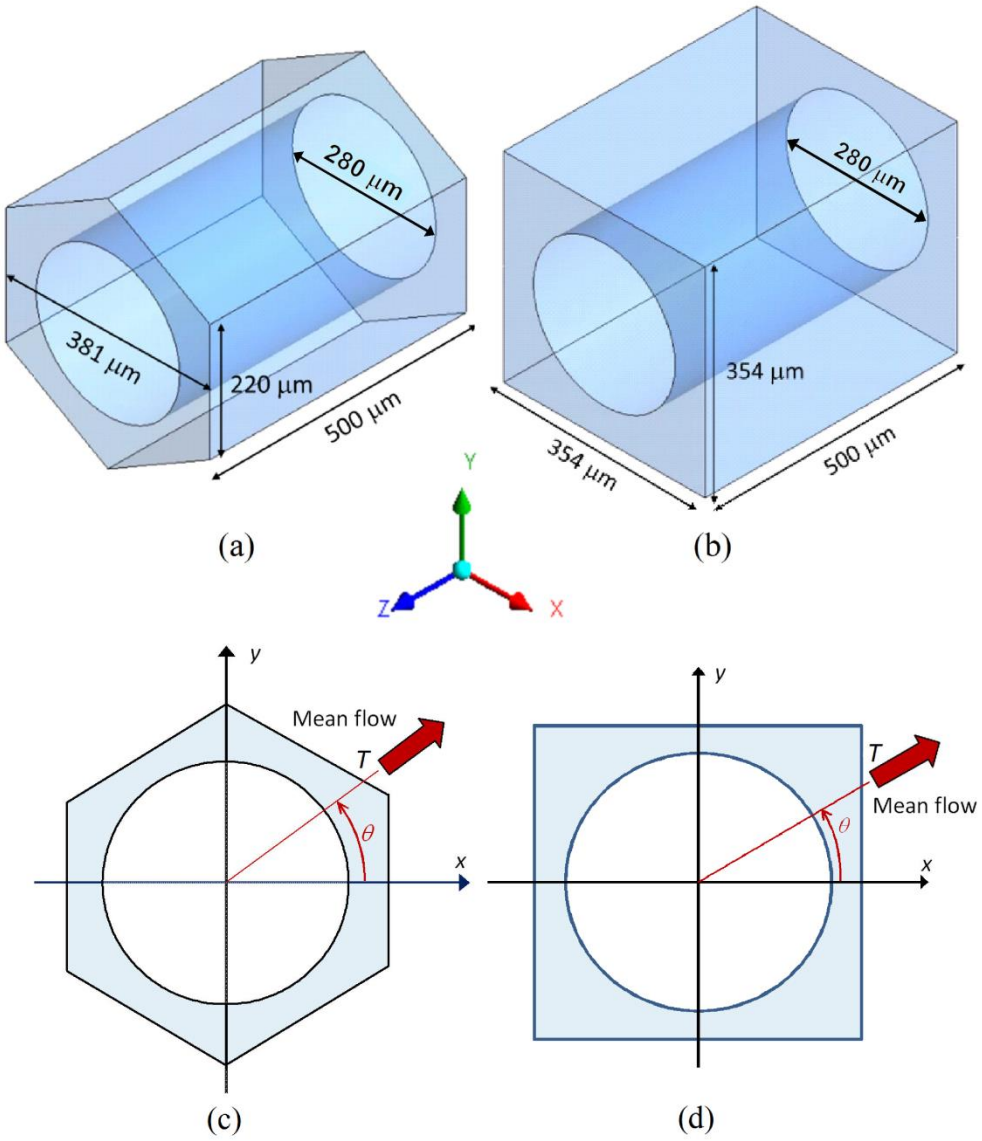

3

4 **Figure 2:** Geometries of a hexagonal regular lattice (a, c) and a square regular lattice (b, d) with porosity ε=0.5. (a), (b) 3-D unit cells (computational domains); (c), (d) 2-D cross sections. The mean flow direction T and the flow attack angle θ are indicated.

4.1 Main definitions

In the present study, the Reynolds number along a generic direction s of unit vector $\vec{\sigma}$ was defined as:

$$Re_s = \frac{\rho \cdot \langle u_{s,sup} \rangle \cdot D_h}{\mu} \tag{2}$$

where ρ is density, μ is dynamic viscosity, $\langle u_{s,sup} \rangle$ (mean superficial velocity along s) is the volume average of the superficial velocity component $u_{s,sup} = \vec{u} \cdot \vec{\sigma}\varepsilon$ along the same direction and D_h is the hydraulic diameter:

$$D_h = \frac{4 \cdot V}{S} \tag{3}$$

173 V being the volume of fluid and S the wet surface in the computational domain. The *interstitial*
174 velocity, if required, can be obtained dividing the superficial velocity by the porosity ε.
175 The Darcy friction coefficient f_s relative to the generic direction s was defined with reference to the
176 above hydraulic diameter as:

$$f_s = \frac{|\mathrm{d}p/\mathrm{d}s| \cdot 2D_h}{\rho \cdot \langle u_s \rangle^2} \tag{4}$$

177 where p is pressure. The hydraulic permeability K_s was defined as:

$$K_s = \frac{\mu \cdot \langle u_s \rangle}{|\mathrm{d}p/\mathrm{d}s|} \tag{5}$$

178 On the basis of definitions (2) and (4), K_s is related to the Darcy friction coefficient f_s by:

$$K_s = \frac{2D_h^2}{f_s Re_s} \tag{6}$$

179 In the literature, the permeability is often expressed in dimensionless form, e.g. as K_s/d^2 (d being the
180 fiber diameter) or by introducing the so called Kozeny "constant" k:

$$k = \frac{\varepsilon^3}{(1-\varepsilon)^2} \cdot \frac{1}{\Sigma^2 K} \tag{7}$$

181 where Σ is the specific surface of the medium particles ($4/d$ for cylinders). Eq. (7) is usually adopted
182 under the assumption of an isotropic permeability, so that the direction subscript "s" is omitted.
183 The *local* shell-side mass transport coefficient U was defined as:

$$U = \frac{J}{C_{wall} - C_{bulk}} \tag{8}$$

184 where J is the local molar flux at the wall, C_{wall} is the local solute concentration at the wall and C_{bulk}
185 is the bulk concentration, defined as the mass flow – weighted average of the solute concentration on
186 an arbitrary cross section. In the present simulations, this section was defined as the intersection of
187 the computational domain with an oblique plane, so that a velocity component orthogonal to the
188 section always exists, independent of the flow direction (purely axial, purely transverse or mixed),
189 thus allowing a bulk concentration to be computed.
190 An average mass transfer coefficient can be defined in different ways. A first possible definition, very
191 common in the literature, is

$$U^{(1)} = \overline{U} = \overline{\left(\frac{J}{C_{wall} - C_{bulk}}\right)} \tag{9}$$

192 i.e., as the surface average of the local U over the walls (wall-average is denoted, here and in the
193 following, by an overbar). A second possible definition is

$$U^{(2)} = \frac{\bar{J}}{\overline{C_{wall}} - C_{bulk}} \tag{10}$$

which does not make any use of a local U.

Consistently, also the average Sherwood number can be calculated either as:

$$Sh^{(1)} = U^{(1)} \frac{D_h}{D} \tag{11}$$

or as

$$Sh^{(2)} = U^{(2)} \frac{D_h}{D} \tag{12}$$

where D is the diffusion coefficient of the solute.

Merits and demerits of the two definitions in similar configurations were reviewed, for example, by La Cerva *et al.* (39). If Dirichlet boundary conditions (imposed concentration at the wall) are used, then the two definitions coincide, i.e. $U^{(1)}=U^{(2)}$ and thus $Sh^{(1)}=Sh^{(2)}=Sh^{(CW)}$. On the other hand, if the boundary conditions are of the Neumann type (imposed mass flux at the wall), the two definitions yield more or less different values of the average U and thus $Sh^{(1)}\neq Sh^{(2)}$, as will be discussed in greater detail in Section 3.2.

In the fiber bundle, purely axial flow is obtained if only the pressure gradient along the axial (z) direction, $|dp/dz|$, is nonzero. To simulate cross-flow, the simultaneous presence of multiple pressure gradients in different directions must be imposed. The cross-flow attack angle θ is defined as the angle in the xy plane between the mean flow direction T and the x-axis, as illustrated in **Figure 2 (c,d)**.

Besides the longitudinal Reynolds number Re_z, computed from the mean superficial velocity $\langle u_z \rangle$ along the axial direction z, also a transverse Reynolds number Re_T can be defined using the mean superficial velocity $\langle u_T \rangle$ resulting from the mean superficial velocities $\langle u_x \rangle$, $\langle u_y \rangle$

$$\langle u_T \rangle = \langle u_x \rangle \cdot \cos\theta + \langle u_y \rangle \cdot \sin\theta \tag{13}$$

4.2 Governing equations

4.2.1 Continuity and momentum equations

The steady-state continuity and momentum equations for the flow of a Newtonian incompressible fluid are:

$$\vec{\nabla} \cdot \vec{u} = 0 \tag{14}$$

$$\rho \vec{u}\, \vec{\nabla} \cdot \vec{u} = -\vec{\nabla} p + \mu \nabla^2 \vec{u} \tag{15}$$

where $\vec{u}$ is velocity. The physical properties (density and viscosity) were assumed to be constant since their changes, associated with changes in concentration, were estimated to be negligible. All simulations were restricted to flow rates at which steady laminar flow is expected, as justified by the nature of the problem investigated (mass transfer through hollow fiber membranes).

4.2.2 Transport equation of solute concentration

The following convection-diffusion transport equation was assumed to govern the concentration field:

$$\vec{u} \cdot \vec{\nabla} C = D\nabla^2 C \tag{16}$$

where C is the concentration of the solute (in mol/m^3) and D is its diffusion coefficient. Heat transport would be governed by a formally identical equation with C replaced by the temperature T and D replaced by the thermal diffusivity α.

4.2.3 Treatment of periodicity

In the UC approach, periodic boundary conditions are imposed to all variables between opposite boundaries. On the other hand, it is necessary to allow for a streamwise variation of pressure, due to the hydraulic resistance of the medium, and of bulk concentration, due to solute inflow or outflow through the membrane fiber wall. This apparent contradiction is managed as follows (37-38).

Consider first the hydrodynamic issue, involving pressure. In the fully-developed region of a bundle, the static pressure $p(x, y, z)$ can be split into a spatially periodic component $\tilde{p}(x, y, z)$ whose spatial distribution repeats itself identically in each UC, and a large scale component $p_{LS}=-G_p s$, where s is a coordinate along the main flow direction whose unit vector is $\vec{\sigma}$ and $G_p=-\mathrm{d}p_{LS}/\mathrm{d}s=-\vec{\nabla}p_{LS}\cdot\vec{\sigma}$. By substituting $\tilde{p}-G_p s$ for p in Eq. (15), this becomes

$$\rho\vec{u}\,\vec{\nabla}\cdot\vec{u} = -\vec{\nabla}\,\tilde{p} + \mu\nabla^2\vec{u} + G_p\vec{\sigma} \tag{17}$$

Eq. (17) is similar to Eq. (15), but a body force per unit volume (driving pressure gradient) acting along the direction $\boldsymbol{\sigma}$ is now present in the right hand side, and the pressure p is replaced by its periodic component $\tilde{p}$. In the simulations, the driving pressure gradient is dynamically adjusted (in module and direction) obtaining a desired mean velocity (in module and direction).

A similar treatment is adopted for the concentration C. By definition of fully developed conditions, $C(x, y, z)$ can be split into a periodic component $\tilde{C}(x, y, z)$ and a large scale component $C_{LS}(x, y, z)=G_c\cdot s$, with $G_c=\mathrm{d}C_{LS}/\mathrm{d}s=\vec{\nabla}C_{LS}\cdot\vec{\sigma}$. G_c can be either positive (net inflow of the solute into the solution) or negative (net outflow of the solute from the solution).

By substituting $\tilde{C}+G_c s$ for C in Eq.(16), the following transport equation is obtained:

$$\vec{u} \cdot \vec{\nabla} \tilde{C} = D\nabla^2 \tilde{C} + S_c \tag{18}$$

in which the source (sink) term, a local quantity, is S_c=–$G_c u_s$. From a global balance of solute in the computational domain it is easily demonstrated that the source term can be written as:

$$S_c = -\left(\frac{\bar{J}S}{V}\right) \cdot \frac{u_s}{\langle u_s \rangle} \tag{19}$$

in which brackets indicate average over the computational domain; $\bar{J}$ is the surface-averaged mass flux of solute in mol/(m^{2}s) from the membrane fiber walls into the fluid, which can either be imposed in the simulations (if Neumann boundary conditions are used) or computed as part of the solution (if Dirichlet or Robin conditions hold). Note that the quantity $\bar{J}S/V$ is the average value of the source term, in mol/(m^{3}s), while the last fraction in Eq. (19) is a dimensionless local correction. This approach, apart from numerical approximations, guarantees solute mass conservation: the mean value of the bulk concentration adopted as the initial guess is conserved through the simulation.

4.3 Boundary conditions and physical properties

The CFD model was implemented in the finite volume code Ansys-CFX 18®.

The fluid was representative of the dialysate in a haemodialysis module. For simplicity, solution properties were set equal to those of pure water at 25°C (40), i.e. density ρ=997 kg/m^3 and viscosity μ=8.89·10^{-4} Pa·s. The diffusivity D of the solute in the solution was that of urea (41), i.e. 1.81·10^{-9} m^2/s, so that the Schmidt number, $\mu/(\rho D)$, was 493.

Regarding hydrodynamics, the cylindrical surfaces representing mass exchange walls were treated as no slip walls. Regarding mass transfer, in most cases a Neumann boundary condition was adopted, with an arbitrarily set value for the mass flux (Sherwood numbers are not affected by this value). In some runs, Dirichlet boundary conditions were also tested (see, for example, Section 3.2), with the concentration at the walls set at an arbitrary uniform value (the value chosen does not affect U). In both cases, the bulk concentration of the dialysate was set at a further arbitrary value. As discussed in the previous Section 2.4, periodicity conditions were imposed for all quantities, including $\tilde{p}$ and $\tilde{C}$, at the opposite boundaries of the computational domain.

All simulations were run in double precision and were interrupted as the dimensionless residuals of all quantities decreased below 10^{-12}, which is a very tight convergence criterion.

4.4 Grid independence

Several grid-independence tests were conducted. As an example, **Figure 3** reports comparative results obtained for a regular hexagonal array of fibers using either triangular or quadrilateral prisms as finite

volumes (FV) and letting their total number N_{tot} range from ~3×2000 to ~3×128,000 (as mentioned above, the 2-D grid in the *xy* plane of the cross section is made up of $N_{tot}/3$ triangles or quadrangles). Two combinations of Re_z (Reynolds number along the axial direction *z*) and Re_T (Reynolds number in the plane of the cross section) were considered, namely, (Re_z=5, Re_T=0.5) or (Re_z=50, Re_T=5). The flow attack angle θ in the cross section (see Figure 3) was arbitrarily set to 30°.

In **Figure 3**, the axial and transverse friction coefficients and the mean Sherwood number $Sh^{(CW)}$ (computed for uniform wall concentration) are shown as functions of the number of finite volumes in the cross section of the computational domain The friction coefficients f_z and f_T are multiplied by the relevant Reynolds number Re_z, Re_T in order to account for the common 1/Re dependence.

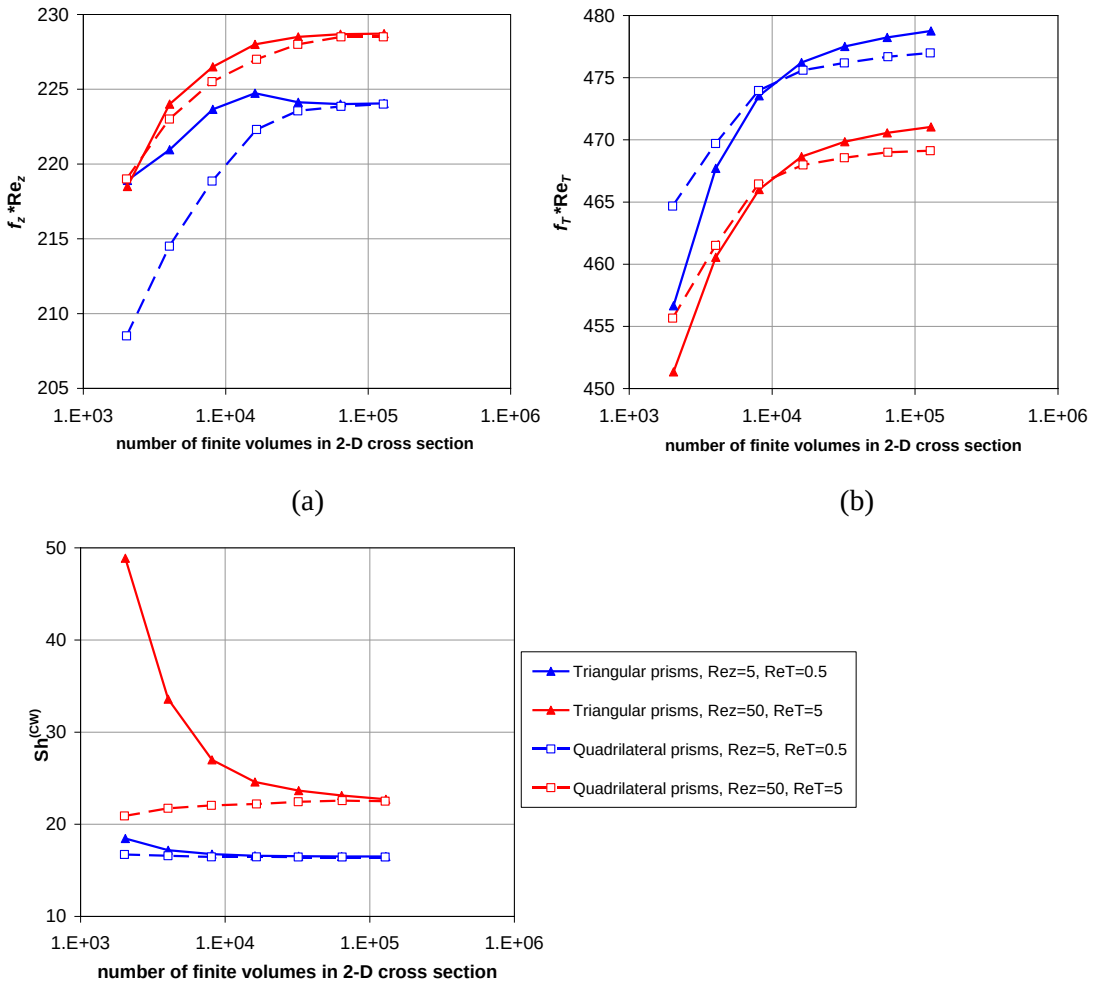

Figure 3: Results of the grid-independence study conducted for a regular hexagonal array for (Re_z=5, Re_T=0.5) or (Re_z=50, Re_T=5). (a) Axial friction coefficient, (b) transverse friction coefficient; (c) mean Sherwood number $Sh^{(CW)}$ (uniform wall concentration). Flow attack angle θ=30°.

It is clear from these results that the predictions converge to about the same values as the number of finite volumes in the grid increases both triangular and quadrilateral prisms; however, especially for the Sherwood number, convergence is achieved earlier (i.e., for a smaller number of volumes) for

quadrilateral prisms, which were therefore chosen in the subsequent simulations. With this choice, ~16,000 volumes in the *xy* plane (i.e. ~48,000 overall volumes) were sufficient to achieve a discrepancy below ~1% on all quantities with respect to the finest grid. However, due to their rather inexpensive nature, simulations were conducted using grids similar to the finest tested above. Thus, the number of finite volumes in the final grids was 316,800 for the hexagonal arrays and 300,000 for the square array.

3. Results

A large number of simulations were conducted by letting the longitudinal and transverse flow Reynolds number Re_z, Re_T and the flow attack angle θ vary. For each set of input data, the axial and transverse Darcy friction coefficients (or Darcy permeabilities) and the average Sherwood number were reported as the main performance parameters.

3.1. Purely axial flow

In purely axial flow, only a pressure gradient along the *z* direction was applied. **Figure** reports the Darcy friction coefficient (f_z) predicted as a function of Re_z for both the hexagonal and the square configurations.

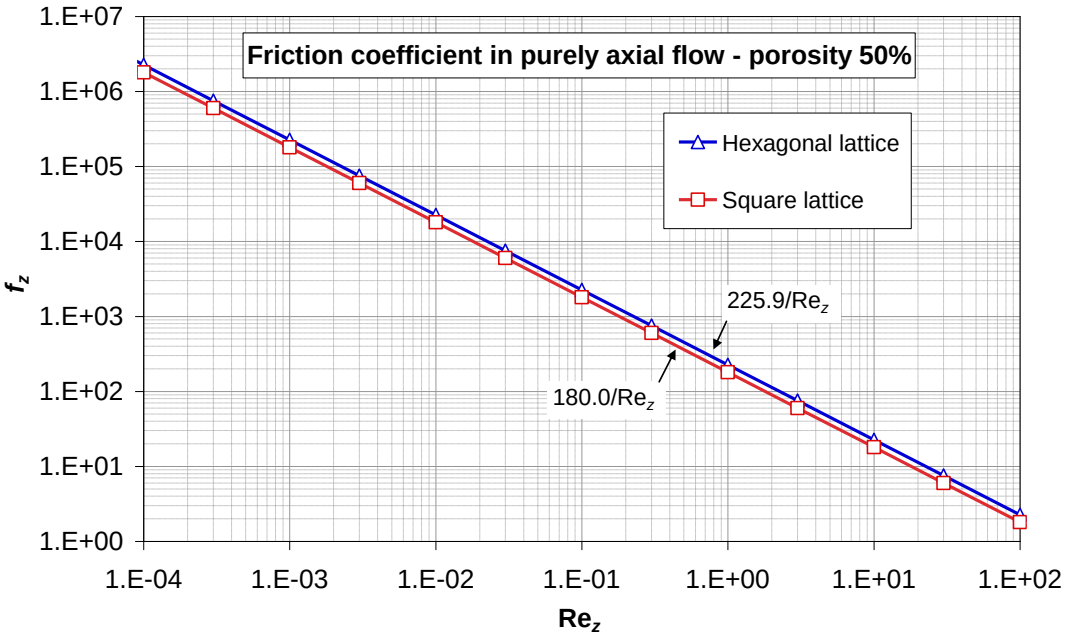

Figure 4: Darcy friction coefficient (f_z) as a function of the longitudinal Reynolds number (Re_z) for hexagonal and square regular lattices.

It can be observed that, for the same porosity, different regular arrangements of the fibers yield fairly different values of the friction coefficient, the larger (~23%) being associated with the hexagonal

lattice. For both configurations f_z follows almost exactly a Re_z^{-1} trend, so that the permeability K_z, which, according to eq. (7), is proportional to $(f_z \cdot Re_z)^{-1}$, does not depend on Re_z; values of $f_z \cdot Re_z$ and K_z are reported in the first two rows of **Table 1**.

Table 1: Product $f_z \cdot Re_z$, permeability K_z, Kozeny's k and average Sherwood numbers predicted for regular lattices in purely axial flow.

Geometry	Hexagonal	Square
$f_z \cdot Re_z$ [-]	226	180
K_z [m^2]	$7.60 \cdot 10^{-10}$	$9.54 \cdot 10^{-10}$
Kozeny's k [-]	3.57	2.88
$Sh^{(1)}$, uniform wall mass flux [-]	9.90	5.64
$Sh^{(2)}$, uniform wall mass flux [-]	9.86	5.15
$Sh^{(CW)}$, uniform wall concentration [-]	9.90	5.82

A comparison of the results of this work with the previous literature can be conducted using the Kozeny "constant" k defined by Eq. (7), which is not affected by the fiber size (third row of **Table 1**). For the present conditions (purely axial flow in regular lattices), simulations gave $k \approx 3.57$ for the hexagonal array and ≈2.88 for the square array. These results compare favourably with the values reported in the literature on flow in fibrous media. Happel (18) developed a simplified analytical model independent of the arrangement of the fibers; for flow parallel to cylinders, at a porosity of 50%, the computed value of k was 3.67. Sparrow and Loeffler (42) obtained analytical solutions for the longitudinal laminar flow between cylinders arranged either in hexagonal or in square arrays, predicting values of k of about 3.5 and 2.9, respectively. Skartsis *et al*. (43) reported experimental and theoretical results obtained by several authors for axial flow through aligned cylinder arrangements, including Larson and Higdon's (44) numerical solution for square arrays, which, at a porosity of 50%, predicts $k \approx 2.75$.

In regard to mass transfer, as expected for purely axial flow, the computed Sherwood number remains constant as the longitudinal Reynolds number (Re_z) increases. Values of $Sh^{(1)}$ and $Sh^{(2)}$ computed for uniform wall mass flux boundary conditions are reported in the fourth and fifth rows of **Table 1**, while the value of $Sh^{(CW)}$ (computed for uniform wall concentration boundary conditions) are reported in the last row. It can be observed that, for the hexagonal configuration, the Sherwood number is much higher than for the square one, and the different Sherwood numbers are much closer to one another.

Experimental results on shell-side mass (or heat) transfer in fiber bundles are affected both by entry effects and by bundle irregularities causing transverse flow. Therefore, experiments depart largely from the assumption of fully developed and purely axial flow and generally show some degree of Reynolds number dependence in the Sherwood number (20).

3.2. Purely transverse flow

In transverse flow, only a driving pressure gradient lying in the cross-section plane was applied, having, in general, both *x* and *y* components. Simulations were conducted for both regular hexagonal and regular square lattices. In either case, the (directional) permeability K_T and the Sherwood number Sh are expected to depend both on the transverse flow Reynolds number Re_T and on the mean flow attack angle θ. The simulations conducted in this study predicted a complex behaviour, as illustrated in the following figures.

3.2.1. Hexagonal lattice

Note that, in a regular hexagonal lattice, the angular dependence of any quantity is periodic with a period of 60°, but only flow attack angles between 0 and 30° need to be explicitly studied because the range 30-60° can be obtained by a symmetric reflection about the direction θ=30°.

In regard to friction, up to a transverse flow Reynolds number $\mathrm{Re}_T \approx$5-10 the transverse Darcy friction coefficient f_T is about the same at all flow attack angles θ and decreases almost exactly as $1/\mathrm{Re}_T$. This shows that, at sufficiently low Reynolds numbers, the fiber lattice is hydraulically isotropic, and the flow is self-similar. In this range, f_T can be approximated as $477/\mathrm{Re}_T$. At higher Re_T, as inertial effects become significant, f_T departs from the $(\mathrm{Re}_T)^{-1}$ behaviour and starts to depend on θ. This behaviour is illustrated in **Figure 5(a)**, which reports f_T (normalized by $477/\mathrm{Re}_T$) as a function of Re_T for different values of θ. It can be observed that, for θ=10°-30°, the friction coefficient at $\mathrm{Re}_T=10^2$ is about twice that predicted by extrapolating the low-Reynolds number behaviour.

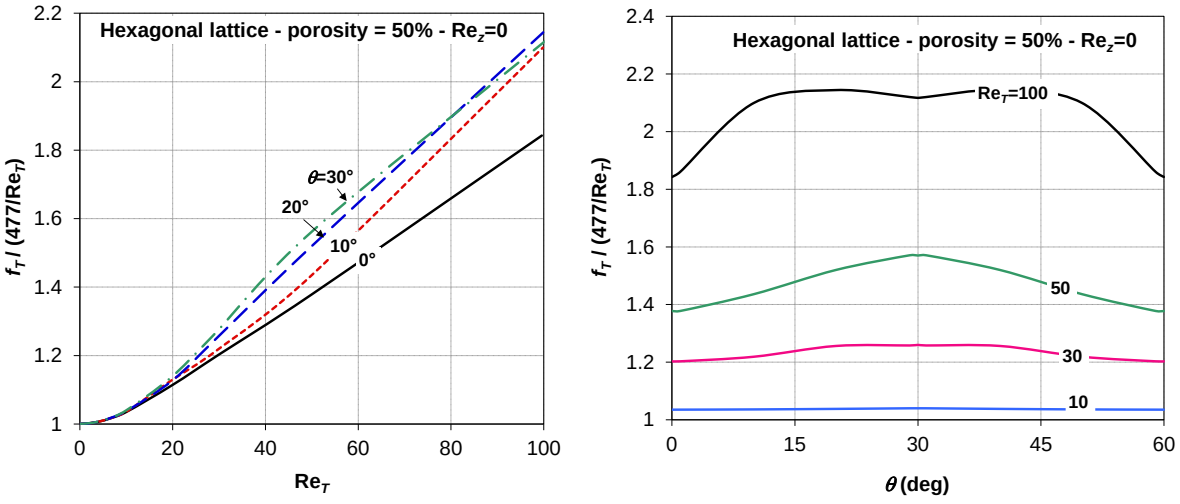

Figure 5: Friction coefficient f_T (normalized by $477/\mathrm{Re}_T$) for pure cross flow in a hexagonal lattice of porosity ε=0.5. (a) f_T as a function of the transverse flow Reynolds number Re_T at different flow attack angles θ; (b) f_T as a function of θ (in the periodic range 0-60°) at different values of Re_T.

The dependence of the friction coefficient on the flow attack angle is better evidenced in **Figure 5(b)**, which reports f_T (normalized by $477/\mathrm{Re}_T$) as a function of θ for different values of the transverse flow Reynolds number Re_T. Consistently with the above remarks, up to $\mathrm{Re}_T \approx 5\text{-}10$ there is practically no influence of θ, whereas, for larger Re_T, f_T develops an absolute minimum for $\theta=0°$ (or 60°) and a maximum for $\theta=30°$, which are the directions of symmetry of the hexagonal lattice. As Re_T increases further, the minimum at 0° - 60° persists but a secondary minimum develops for $\theta=30°$, while two maxima appear for $\theta° \approx 15°$ and 45°. The peaking factor (angular maximum/angular average), however, remains small, i.e. the hexagonal lattice remains hydraulically almost isotropic up to relatively high values of Re_T.

In regard to mass transfer, **Figure 6** reports the various average Sherwood numbers defined in Section 2.2 for a hexagonal lattice at the reference porosity of 0.5. Two flow attack angles are considered, $\theta=0°$ and $\theta=30°$, and the transverse flow Reynolds number Re_T varies over a large interval from 10^{-4} to 10^2, covering six orders of magnitude. The results include those for uniform wall mass flux, for which the two different averages $\mathrm{Sh}^{(1)}$ and $\mathrm{Sh}^{(2)}$ were reported, and those obtained for uniform wall concentration, for which the two definitions coincide and thus a single Sh exists, indicated here as $\mathrm{Sh}^{(CW)}$.

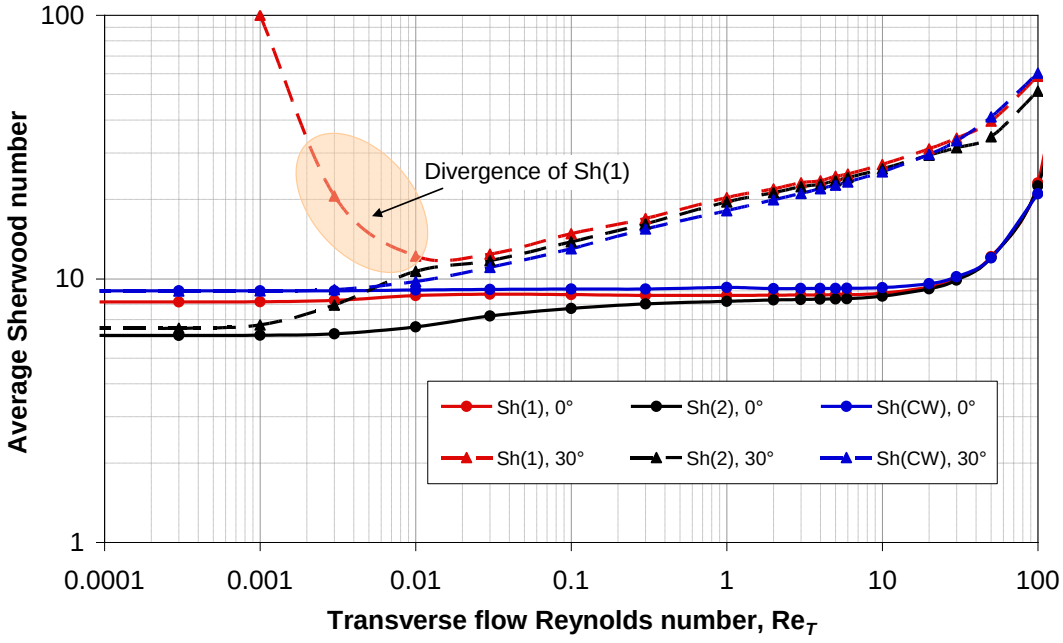

Figure 6: Average Sherwood numbers computed as functions of the transverse flow Reynolds number for purely transverse flow in a hexagonal lattice with $\varepsilon=0.5$ and $\theta=0$ or 30°. Results include the case of imposed wall mass flux, for which $\mathrm{Sh}^{(1)}$ and $\mathrm{Sh}^{(2)}$ differ, and that of imposed wall concentration, for which $\mathrm{Sh}^{(1)}$ and $\mathrm{Sh}^{(2)}$ coincide and are denoted as $\mathrm{Sh}^{(CW)}$.

For the case θ=0, $Sh^{(CW)}$ remains practically constant at a value of ~9 up to Re_T≈10 and then increases, attaining values of ~12 for Re_T=50 and ~21 for Re_T=100. For imposed wall mass flux, $Sh^{(1)}$ remains slightly lower than $Sh^{(CW)}$ (by ~10%) in the whole Reynolds number range, and thus follows the same trend. The only feature worth noting is a slight increase, from 8.2 to 8.8, in the range Re_T≈0.003-0.03. $Sh^{(2)}$ remains significantly lower than $Sh^{(1)}$ (by ~25-30%) in the very low Reynolds number range Re_T<~0.003, while in the range Re_T≈0.003-10 the difference shrinks and becomes negligible for Re_T≥10. None of the defined average Sherwood numbers follows a power law trend in any Re_T interval.

For θ=30°, in the range Re_T>~0.01 all three Sherwood numbers follow the same trend, characterized by an increasing power-law trend of exponent ~1/3 which persists up to Re_T≈20-30. The slope of all three $Sh(Re_T)$ curves increases for larger Re_T; for example, $Sh^{(2)}$ is ~26 for Re_T=10, ~36 for Re_T=50 and ~52 for Re_T=100.

At very low Reynolds numbers (≤0.01, say), the scenario for θ=30° is more complex. In particular, $Sh^{(1)}$ attains unphysically large values and diverges for Re_T≈0.001. The reason for this behaviour is made clear by the examination of **Figure 7**, which reports maps of the dimensionless concentration in the UC of a regular hexagonal lattice for a porosity of 0.5, purely transverse flow with an attack angle of 30°, and three different values of the transverse flow Reynolds number (0.001, 0.003 and 0.01, respectively). The dimensionless concentration is defined here as

$$C^* = \frac{\tilde{C} - C_{bulk}}{\overline{C_{wall}} - C_{bulk}} \tag{20}$$

(see Section 2.3 for the various definitions).

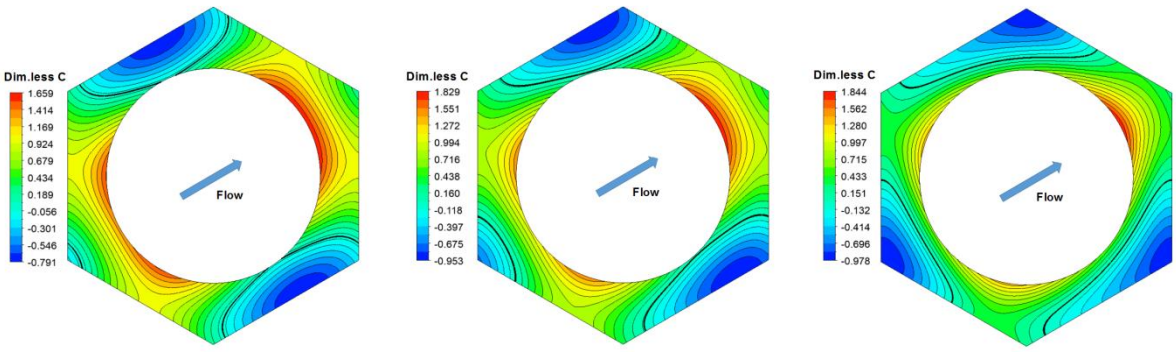

(a) (b) (c)

Figure 7: Dimensionless concentration in the UC of a hexagonal lattice with ε=0.5 for θ=30° and three values of the transverse flow Reynolds number: (a) Re_T=0.001; (b) Re_T=0.003; (b) Re_T=0.01. The thick line indicates the bulk concentration.

In each map the thick line represents the iso-concentration curve C^*=0, i.e. $\tilde{C}$=C_{bulk}. At sufficiently high Re_T – e.g. 0.01, map (c) – the concentration at the wall is everywhere larger than C_{bulk}, so that the local mass transfer coefficient U in Eq. (9) is everywhere positive and well defined and can be averaged over the wall to obtain $U^{(1)}$ and $Sh^{(1)}$. On the other hand, at very low Re_T – e.g. 0.001, map (a) – the iso-line $\tilde{C}$=C_{bulk} intersects the wall, so that some regions of this latter exhibit C_{wall}>C_{bulk} and thus a positive value of U; other regions exhibit C_{wall}<C_{bulk} and thus a *negative*, unphysical value of U; and, at some points, one has C_{wall}=C_{bulk}, so that U diverges. Averaging such a distribution of U over the wall provides, of course, meaningless results. Finally, map (b), which is for Re_T=0.003, exhibits an intermediate behaviour: the isoline $\tilde{C}$=C_{bulk} does not quite touch the wall, so that U remains positive and limited everywhere, but the very small difference existing at some points between the wall and bulk concentration causes very high local values of U and an unphysically high value of $Sh^{(1)}$, as confirmed by the corresponding point in **Figure 6**.

The inadequacy of the usual definition of local mass (or heat) transfer coefficient, especially in low-Reynolds number flows, has already been pointed out by our research group (39) and mainly arises from putting together into a single definition like eq. (8) local quantities (J, C_{wall}) and a global quantity (C_{bulk}).

Figure 7 also allows one to appreciate how the flow, even at such low Reynolds numbers, significantly affects the scalar distribution: at Re_T=0.001, map (a), this is almost symmetric between the upstream and downstream regions of the wall, whereas at Re_T=0.01, map (c), the effects of advection breaks the above symmetry and leads to a markedly asymmetric scalar distribution. Of course, this is due to the high Schmidt number (493): the transverse Péclet number, $Re_T \cdot Sc$, is 0.493 in case (a) and 4.93 in case (c), values which are small but not negligible. Note that, even for $Re_T \to 0$, the concentration distribution does *not* tend to the centro-symmetric configuration that would be observed in pure diffusion or purely axial flow: the flow direction and that orthogonal to it remain characterized by completely different scalar distributions. The complex way in which the cross flow deforms the iso-concentration curves is the reason for the complex and non-monotonic behaviour exhibited by the Sherwood number as Re_T varies (even at very low values, as evidenced for the hexagonal case in **Figure 6**).

The simultaneous dependence of mass transfer on transverse Reynolds number and flow attack angle is better evidenced in **Figure 8**. $Sh^{(2)}$ was chosen as the most representative mass transfer quantity because, as observed above, $Sh^{(1)}$ may completely lose significance under certain circumstances, notably involving very low Reynolds numbers, whereas $Sh^{(CW)}$ corresponds to boundary conditions (uniform concentration at the walls),) which are rarely approximated in mass transfer units like those considered here (e.g. hollow-fiber bundles).

Figure 8(a) reports $Sh^{(2)}$ as a function of Re_T for four values of θ (0°, 10°, 20° and 30°). It can be observed that, as already discussed in commenting **Figure 6**, for θ=0° $Sh^{(2)}$ remains low (~6-8, close to its limiting value for $Re_T \rightarrow 0$) up to $Re_T \approx 10$, and then increases only moderately attaining a value of ~21 for Re_T=100. For any other flow attack angle considered, $Sh^{(2)}$ grows rapidly in the interval Re_T=0~10 and then continues to increase. The highest values of $Sh^{(2)}$ are attained for flow attack angles of ~10°-20°. Therefore, the Sherwood number is lower in the symmetric directions 0° and 30° than at intermediate angles.

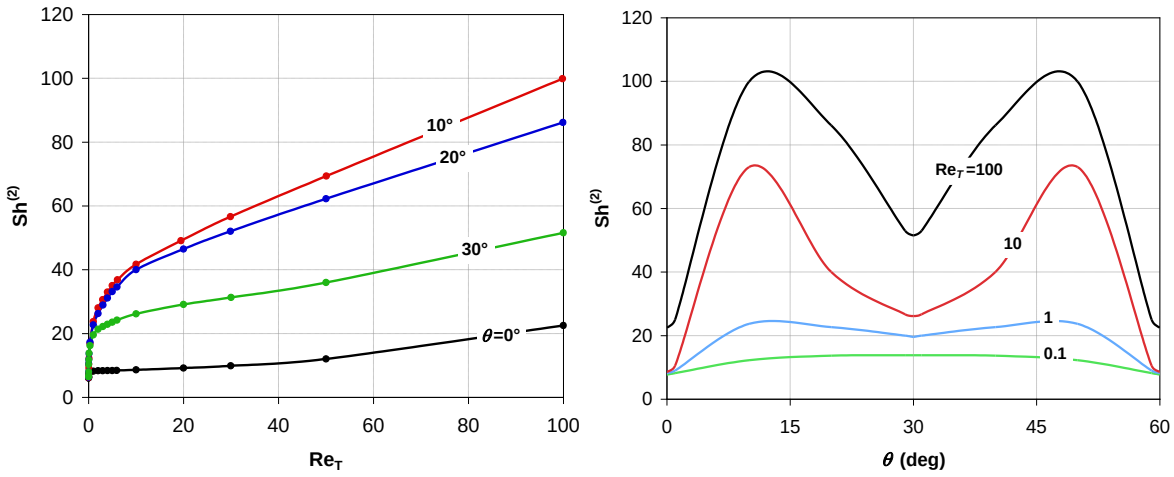

Figure 8: Average Sherwood number $Sh^{(2)}$ for pure cross flow in a regular hexagonal lattice of porosity ε=0.5. (a) $Sh^{(2)}$ as a function of the transverse flow Reynolds number Re_T at different flow attack angles angles θ; (b) $Sh^{(2)}$ as a function of θ (in the periodic range 0-60°) at different values of Re_T.

Figure 8(b) reports $Sh^{(2)}$ as a function of θ for four values of Re_T (0.1, 1, 10 and 100). For clarity purposes, the whole periodic range θ=0-60° is shown although, of course, the profiles of all quantities are symmetric with respect to θ=30° (note that profiles are also necessarily symmetric with respect to θ=0° or 60°). It can be observed that only at very low Reynolds numbers (e.g. Re_T=0.1) the $Sh^{(2)}$ versus θ profile remains about flat whereas, already at Re_T=1, it develops two maxima at $\theta \approx 10$ and 50° and two minima at θ=0°-60° and θ=30° (symmetry directions). The peaking factor (angular maximum/angular average) of $Sh^{(2)}$ becomes as high as ~1.5 at Re_T=100. The comparison of **Figure 8(b)** with **Figure 5(b)** shows that the hexagonal lattice remains hydraulically almost isotropic up to $Re_T \approx 10$ but becomes anisotropic in regard to mass transfer at much lower values of Re_T (0.1-1).

The attitude to transfer mass from the fibers to the solution, and thus the magnitude of the Sherwood number, are strictly related to the shape of the iso-concentration curves for different flow attack angles. For example, for the hexagonal lattice in purely transverse flow at Re_T=1, **Figure 9** reports simplified concentration maps for three values of θ (0°, 15° and 30°). For clarity purposes, a lattice

portion including seven periodic unit cells is shown. Regions in which $C>C_{bulk}$ are indicated in red, regions where $C<C_{bulk}$ in blue.

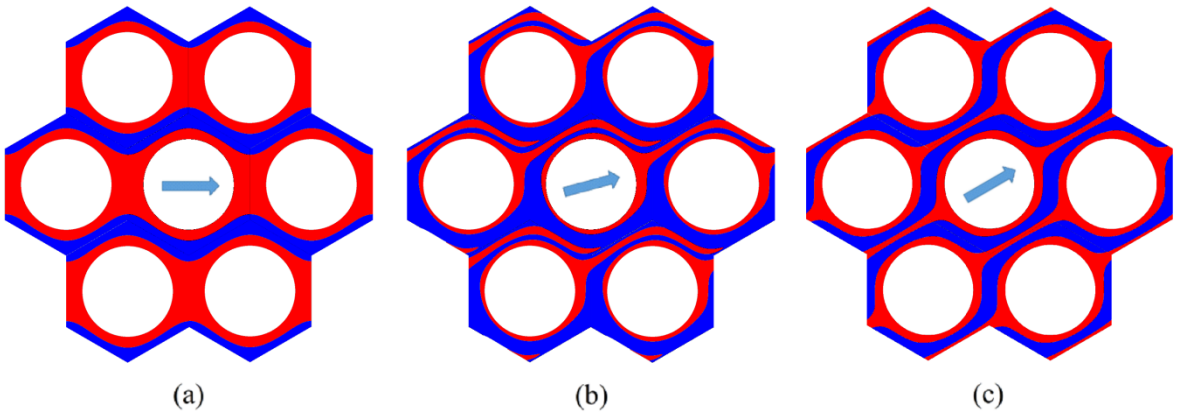

Figure 9: Concentration maps in a hexagonal lattice for purely transverse flow at Re_T=1, uniform wall mass flux and three different flow attack angles: (a) θ=0°; (b) θ=15°; (c) θ=30°. Blue regions; $C<C_{bulk}$; red regions: $C>C_{bulk}$. The arrows indicate the mean flow direction.

For θ=0°, the high-concentration wake that is formed downstream of each obstacle attaches directly to the subsequent obstacle, thus creating a broad region of high C which hinders mass transfer. A similar phenomenon occurs, although to a lesser extent, for θ=30°. On the other hand, for θ=15°, i.e. along a direction which is not a direction of symmetry for the fiber lattice, the high-C wake meanders freely about the fibers until it merges with the bulk flow; this considerably reduces the thickness of the concentration boundary layer and the mean concentration at the fiber wall, thus enhancing mass transfer.

3.2.2. *Square lattices*

Note that, in a regular square lattice, the angular dependence of any quantity is periodic with a period of 90°, but only flow attack angles between 0 and 45° need to be explicitly studied because the range 45°-90° can be obtained by a symmetric reflection about the direction θ=45°.

In regard to friction, up to a transverse flow Reynolds number $Re_T \approx$5-10 the transverse Darcy friction coefficient f_T is about the same at all flow attack angles θ and decreases almost exactly as $1/Re_T$. This shows that, at sufficiently low Reynolds numbers, the fiber lattice is hydraulically isotropic, and the flow is self-similar. In this range, f_T can be approximated as $648/Re_T$ and thus is significantly higher (~36%) than in the hexagonal lattice having the same porosity, a behaviour opposite to that observed for the axial friction coefficient.

At higher Re_T, as inertial effects become significant, f_T departs from the $(Re_T)^{-1}$ behaviour and starts to depend on θ. This behaviour is illustrated in **Figure 10(a)**, which reports f_T (normalized by

648/Re_T) as a function of Re_T for different values of θ. It can be observed that, for θ=15°, the friction coefficient at $Re_T=10^2$ is about twice that predicted by extrapolating the low-Reynolds number behaviour.

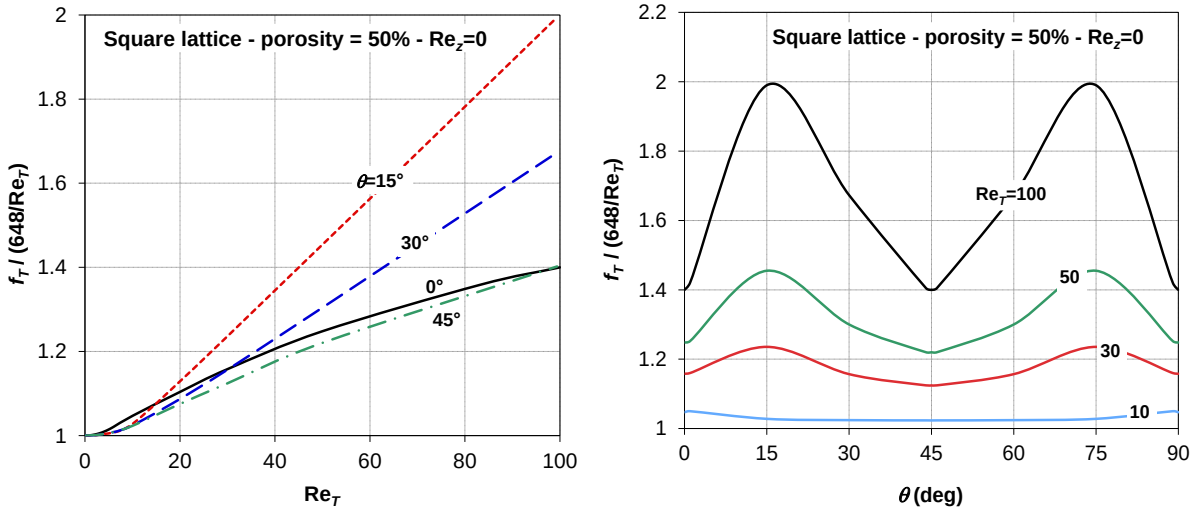

Figure 10: Friction coefficient f_T (normalized by 648/Re_T) for pure cross flow in a square lattice of porosity ε=0.5. (a) f_T as a function of the transverse flow Reynolds number Re_T at different flow attack angles θ; (b) f_T as a function of θ (in the periodic range 0-90°) at different values of Re_T.

The dependence of the friction coefficient on the flow attack angle is better evidenced in **Figure 10(b)**, which reports f_T (normalized by 648/Re_T) as a function of θ for different values of the transverse flow Reynolds number Re_T. Consistently with the above remarks, up to $Re_T \approx 10$ there is little influence of θ (i.e., the lattice behaves almost as a hydraulically isotropic medium); for larger Re_T, f_T develops minima at θ=0°-90° and θ=45°, which are the directions of symmetry of the square lattice, and maxima at intermediate angles (~15°-60°). The peaking factor (angular maximum/angular average) becomes much higher than in the hexagonal lattice, attaining a value of ~1.2 at $Re_T=10^2$. Thus, the square lattice is hydraulically more anisotropic than the hexagonal lattice.

In regard to mass transfer, **Figure 11** reports the various average Sherwood numbers as functions of Re_T. Two flow attack angles are considered, θ=0° and θ=45°, and the transverse flow Reynolds number Re_T varies over a large interval from 10^{-4} to 10^2, covering six orders of magnitude. As in **Figure 6**, the results include those at uniform wall mass flux, with the two different averages $Sh^{(1)}$ and $Sh^{(2)}$, and those at uniform wall concentration, for which the two definitions coincide and thus a single average $Sh^{(CW)}$ exists.

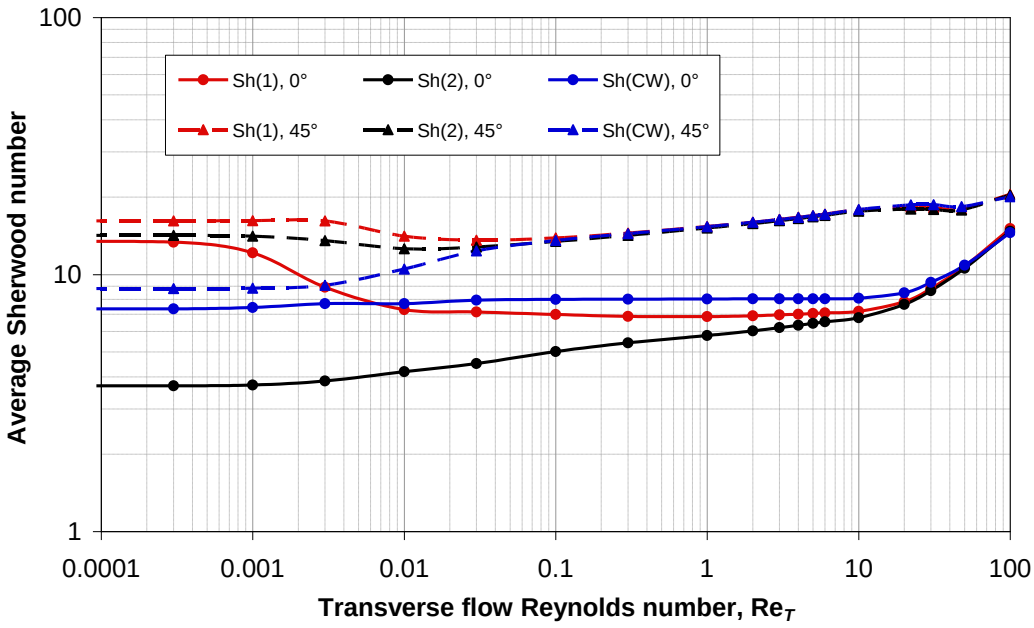

Figure 11: Average Sherwood numbers computed as functions of the transverse flow Reynolds number for purely transverse flow in a square lattice with ε=0.5 and θ = 0 or 45°. Results include the case of imposed wall mass flux, for which $Sh^{(1)}$ and $Sh^{(2)}$ differ, and that of imposed wall concentration, for which $Sh^{(1)}$ and $Sh^{(2)}$ coincide and are denoted as $Sh^{(CW)}$.

For the case θ=0°, $Sh^{(CW)}$ (uniform wall concentration) remains about constant at ~7-8 in the whole range $Re_T \leq 10$ and then increases, attaining values of ~11 for Re_T=50 and ~15 for Re_T=100. Under conditions of uniform wall mass flux, $Sh^{(2)}$ is always less than $Sh^{(CW)}$; it remains about constant only at very low Re_T (~0.001), increases slowly from ~3.8 to ~7 in the range $Re_T \approx 0.001$-10 and then increases more rapidly for higher Re_T, up to ~15 for Re_T=100. $Sh^{(1)}$ starts from relatively high values (~15) for very low Re_T (up to $3 \cdot 10^{-4}$), then decreases and remains about constant at ~7 in the range Re_T=0.01-10, eventually to increase at higher Re_T. The three average Sherwood numbers tend to coincide at the higher Reynolds numbers. As confirmed by an inspection of the concentration distributions predicted for uniform wall mass flux, the anomalous high values of $Sh^{(1)}$ observed at very low Re_T (<0.01) are devoid of physical significance and are rather associated with the iso-line $C=C_{bulk}$ closely approaching the wall, an effect similar to that causing the divergence of $Sh^{(1)}$ in the case of a hexagonal lattice with θ=30° (**Figure 6** and **Figure 7**).

For θ=45°, in the range Re_T>~0.1 all three Sherwood numbers share the same behaviour, characterized by an increasing power-law trend of low exponent which persists up to $Re_T \approx 10$. All three $Sh(Re_T)$ curves flatten in the range Re_T=10-50, to increase again between Re_T=50 and Re_T=100. At the opposite, low Reynolds number, end of the range ($Re_T \leq 0.1$), the three curves depart from one another and tend to different asymptotic values for $Re_T \rightarrow 0$.

The simultaneous dependence of mass transfer on transverse Reynolds number and flow attack angle is better evidenced in **Figure 12**. $Sh^{(2)}$ was chosen as the most representative mass transfer quantity

for the same reasons discussed in the previous section with reference to the hexagonal arrangement.

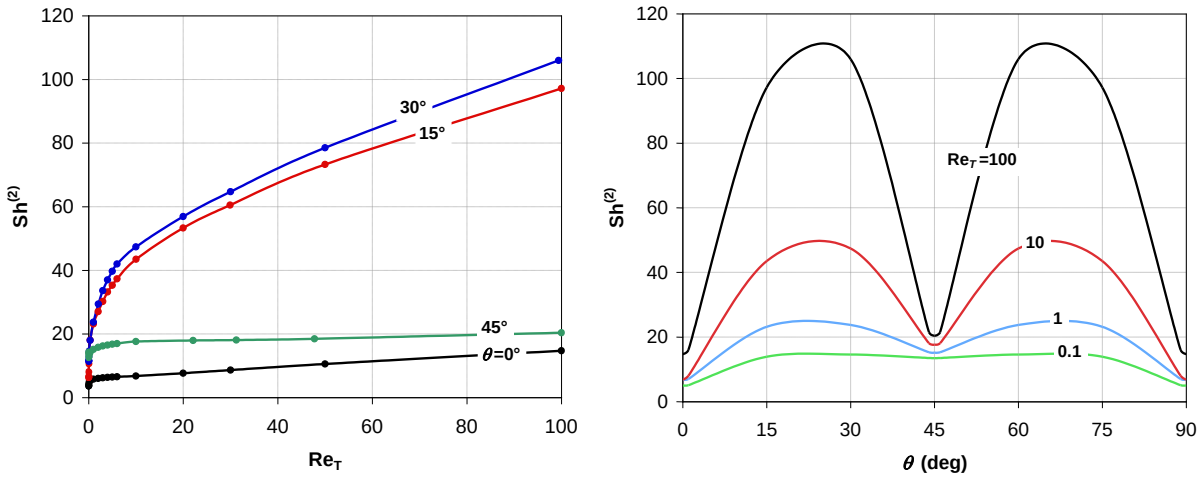

Figure 12: Average Sherwood number $Sh^{(2)}$ for pure cross flow in a regular square lattice of porosity ε=0.5. (a) $Sh^{(2)}$ as a function of the transverse flow Reynolds number Re_T at different flow attack angles θ; (b) $Sh^{(2)}$ as a function of θ (in the periodic range 0-90°) at different values of Re_T.

Figure 12(a) reports $Sh^{(2)}$ as a function of Re_T for four values of θ (0°, 15°, 30° and 45°). For θ=0° and 45° (symmetry directions), $Sh^{(2)}$ increases only moderately with Re_T, while, for intermediate flow attack angles (15° and 30°), it increases much more rapidly.

Figure 12(b) reports $Sh^{(2)}$ as a function of θ for four values of Re_T (0.1, 1, 10 and 100). For clarity purposes, the whole periodic range θ=0-90° is shown although, of course, the profiles of all quantities are symmetric with respect to θ=45° (profiles are also necessarily symmetric with respect to θ=0° or 90°). It can be observed that only at very low Reynolds numbers (e.g. Re_T=0.1) the $Sh^{(2)}$ versus θ profile remains relatively flat whereas, already at Re_T=1, it develops two maxima at θ≈22° and 68° and two minima at θ=0°-90° and θ=45° (symmetry directions). The peaking factor (angular maximum/angular average) of $Sh^{(2)}$ becomes as high as ~1.8 at Re_T=100.

The comparison of **Figure 12(b)** with **Figure 10(b)** shows that, like the hexagonal lattice, also the square lattice remains hydraulically almost isotropic up to relatively high Reynolds numbers (Re_T≈10) but becomes anisotropic in regard to mass transfer at much lower values (Re_T≈0.1-1). The amount of anisotropy is larger than that observed for the hexagonal lattice, as expected in view of the lower degree of symmetry of the square arrangement.

As observed in regard to hexagonal lattices, see **Figure 9**, the physical reason for the strong and non-monotonic dependence of the Sherwood number on the flow attack angle lies in the way θ affects the iso-concentration curves and, in particular, the shape and length of the wake regions downstream of individual fibers. For example, for the square lattice in purely transverse flow at Re_T=1, **Figure 13** reports simplified concentration maps for three values of θ (0°, 15° and 45°). For clarity purposes, a

region including 3×3 fibers is shown. Regions in which $C>C_{bulk}$ are indicated in red, regions where $C<C_{bulk}$ in blue. Remarks similar to those made in regard to **Figure 9** apply.

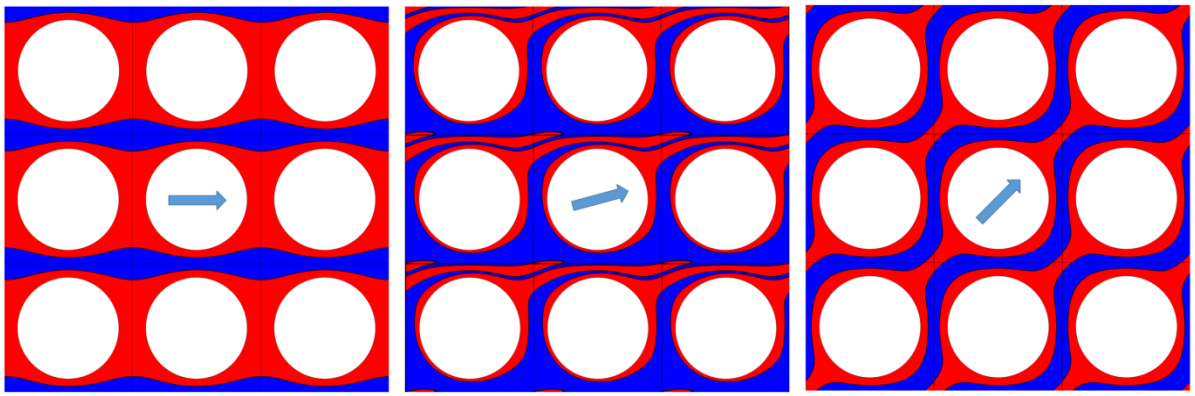

(a) (b) (c)

Figure 13: Concentration maps in a square lattice for purely transverse flow at Re_T=1, uniform wall mass flux and three different flow attack angles: (a) θ=0°; (b) θ=15°; (c) θ=45°. Blue regions; $C<C_{bulk}$; red regions: $C>C_{bulk}$. The arrows indicate the mean flow direction.

3.2.3. Comparison of the two arrangements with each other and with literature results

The angle-averaged Darcy friction coefficients predicted for the hexagonal and the square configurations in purely transverse flow are compared in **Figure 14(a)**, where, for each lattice type, the product $f_T Re_T$ (free from the $1/Re_T$ dependence) is reported as a function of the transverse flow Reynolds number Re_T. It can be observed that, in the whole Re_T range, the friction coefficient attains a higher value in the square lattice than in the hexagonal lattice, a behaviour opposite to that observed for the axial friction coefficient (**Figure 4**). The square/hexagonal f_T ratio is ~1.36 at low Re_T and decreases to ~1.10 at Re_T=100.

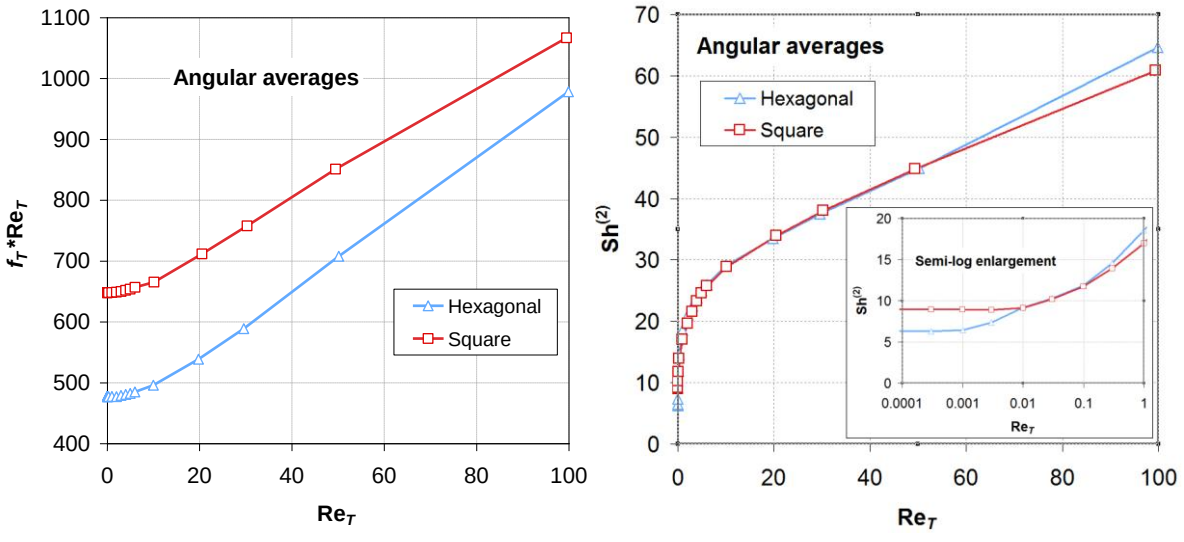

(a) (b)

Figure 14: Angle-averaged Darcy friction coefficient f_T (a) and Sherwood number $Sh^{(2)}$ (b) as functions of the transverse flow Reynolds number Re_T for hexagonal and square regular lattices.

The corresponding angle-averaged values of the Kozeny "constant" k (meaningful only in the $f_T \propto Re_T^{-1}$ range, i.e. up to $Re_T \approx 5$) are 7.61 for hexagonal arrays and 10.36 for square arrays. In the case of flow perpendicular to cylinders at a porosity of 50%, Happel's (18) value of k (obtained by a simplified model which did not distinguish between hexagonal and square arrays) was 5.38. For transverse flow across square arrays of cylinders, Skartsis *et al.* (43) reported experimental and theoretical results of several authors; the k value at a porosity of 50% was ~10.7, which is very close to the present one. For square lattices, the present results are also in good agreement (within 3%) with the semi-analytical solutions obtained by Miyagi (45) for densely packed cylinders and in general agreement with the experimental results of Yeom *et al.* (46) (conducted at porosity values not exactly equal to that considered in this study). The agreement is less satisfactory with results published by Ishimi *et al.* (47), who, on the basis of numerical finite element solutions of the vorticity-stream function equations, reported for a porosity of 0.5 a drag ~29% higher than the present results for the hexagonal lattice and ~13% higher for the square lattice.

The angle-averaged Sherwood number $Sh^{(2)}$ for transverse flow in hexagonal and square arrays are compared in **Figure 14(b)**. In the range Re_T=0.05-50 the two configurations yield very similar values of the Sherwood number; for both arrangements, Sh increases with Re_T following an approximate power law of exponent 0.3. However, at very low Re_T the two curves depart from each other and tend to two different *plateau* values for $Re_T \to 0$ (~6.3 for hexagonal arrays and ~8.9 for square arrays, with a ratio of ~1.4 similar to that observed for the friction coefficient in this range). This can be appreciated in the semi-log inset. Therefore, at low Reynolds number hexagonal arrays yield both lower friction coefficients and lower Sherwood numbers than square arrays.

There are in the literature few mass or heat transfer results (either experimental or computational) obtained under conditions comparable with those of the present study. The Sherwood number computed by Ishimi *et al.* (47) under uniform concentration wall boundary conditions, a porosity of 0.5, a transverse Péclet number of 100 and in the limit of a large array of cylinders (fully developed conditions), was about 8 for the square lattice with a flow attack angle of 0°, in good agreement with the present findings (see **Figure 11** above for Re_T=0.2, i.e. $Pe_T = Re_T Sc \approx 100$), and about 15 for the hexagonal lattice with a flow attack angle of 30°, also in good agreement with the present findings (see **Figure 6** above for Re_T=0.2). Sangani and Acrivos (48) presented semi-analytical solutions for slow flow and heat transfer in square or hexagonal periodic arrays of cylinders but limited the thermal analysis to the case of volumetrically heated cylinders and small Péclet numbers ($Pe^2 \ll 1-\varepsilon$).

3.3. Simultaneous axial and transverse flow

When axial and transverse flow are simultaneously present, the number of parameters to be

considered grows (porosity ε, Reynolds numbers Re_z, Re_T and flow attack angle θ for each lattice type, i.e. hexagonal or square) and a full parametrical study becomes prohibitive. However, some interesting conclusions can be drawn even from results obtained for a fixed porosity (50%) and a few combinations of Re_z, Re_T and θ.

Let us first consider the hexagonal lattice and discuss the way in which the simultaneous presence of an axial flow affects friction and mass transfer characteristics. **Figure 15(a)** compares the transverse friction coefficient (expressed as $f_T Re_T$) as a function of the transverse flow Reynolds number Re_T in the absence of axial flow (Re_z=0) and in the presence of axial flow at Re_z=100. The plot is for θ=10° but a similar trend is obtained for all flow attack angles. It can be observed that the transverse friction coefficient, and thus the transverse permeability K_T (inversely proportional $f_T Re_T$) is completely unaffected by the presence of the axial flow in the whole Re_T range considered, despite the significant value of Re_z. Independent of the presence of axial flow, $f_T Re_T$ departs from its constant, low-Reynolds number value of ~477 only for Re_T>~5-10. Thus, the plot in **Figure 5(a)**, drawn for purely transverse flow, applies also in the presence of an axial flow of arbitrary intensity.

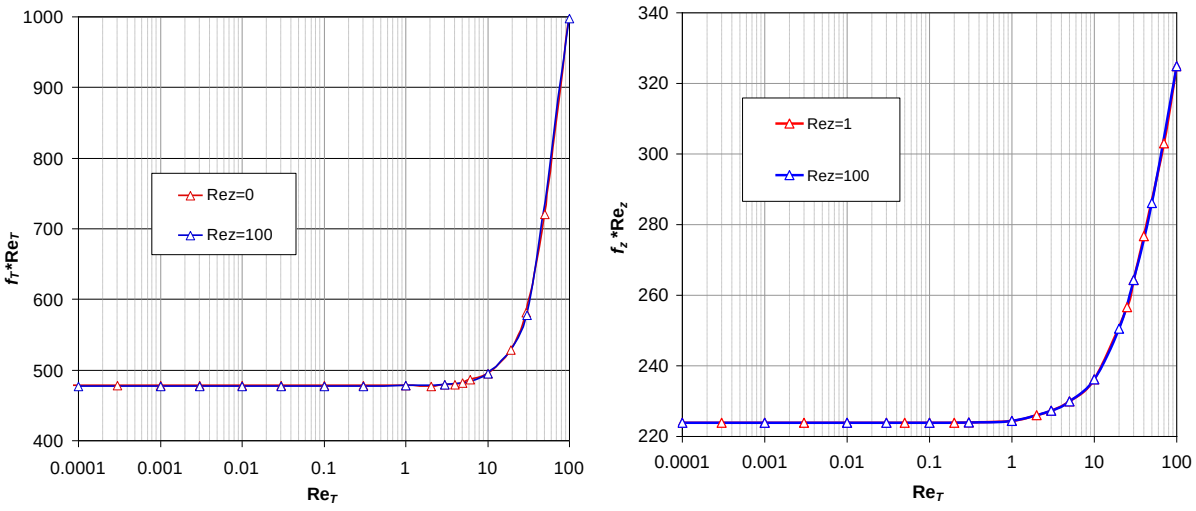

(a) (b)

Figure 15: Hexagonal lattice with ε=0.5 and θ=10°. Comparison of $f_T \cdot Re_T$ (a) and $f_z \cdot Re_z$ (b) as functions of the transverse flow Reynolds number Re_T for different intensities of the axial flow.

For the same configuration (hexagonal lattice with porosity 0.5, flow attack angle θ=10°), **Figure 15(b)** reports the axial friction coefficient, in the form $f_z Re_z$, as a function of the transverse Reynolds number Re_T for two values of Re_z, 1 and 100 (of course, for Re_z=0 the quantity f_z is not defined). It can be observed that, independent of the axial flow intensity, the presence of a transverse flow starts affecting the axial friction coefficient for $Re_T \approx 1$; the presence of cross flow with R_T=10 enhances f_z by ~5% (and thus reduces by the same amount the axial flow rate for any given applied pressure difference), while for Re_T=100 the variation in f_z is as high as ~45%. It is interesting to note that the

relative increase of the axial friction coefficient is associated with the *absolute* intensity of the transverse flow (i.e., with Re_T) and not with its intensity *relative* to the axial flow (i.e., with Re_T/Re_z). Thus, for relatively high axial Reynolds numbers (say, Re_z=100), even a moderate relative transverse flow component (say, 10% of the axial flow, i.e. Re_T=10), as might be caused by an uneven distribution of the bundle porosity or by some undulation of the fibers, would cause an increase of ~5% (from ~224 to ~236, see Figure 15(b)) in $f_z Re_z$ and thus in the axial frictional pressure drop. A qualitatively similar behaviour is obtained also for the square lattice. Plots are not reported here for the sake of brevity.

The behaviour of the average Sherwood number $Sh^{(2)}$, reported in **Figure 16(a)** for the same configuration of **Figure 15** (hexagonal lattice of porosity 0.5 and θ=10°), is more complex. For sufficiently large Re_T, the two curves for transverse and mixed flow are practically coincident, showing that, in this range, mass transfer is controlled exclusively by the transverse flow and not by the axial flow. However, as Re_T decreases below the value (~0.02) at which $Sh^{(2)}$ for purely transverse flow becomes less than the value obtained in purely axial flow ($Sh^{(2)}_{ax}$≈9.85), the mixed-flow $Sh^{(2)}$ curve leaves the pure transverse flow trend and tends to $Sh^{(2)}_{ax}$, becoming practically coincident with it at Re_T<~0.003. In an intermediate range of Re_T (0.003~0.3) the mixed-flow $Sh^{(2)}$ exhibits a transitional behaviour. A similar behaviour is obtained under different flow attack angles.

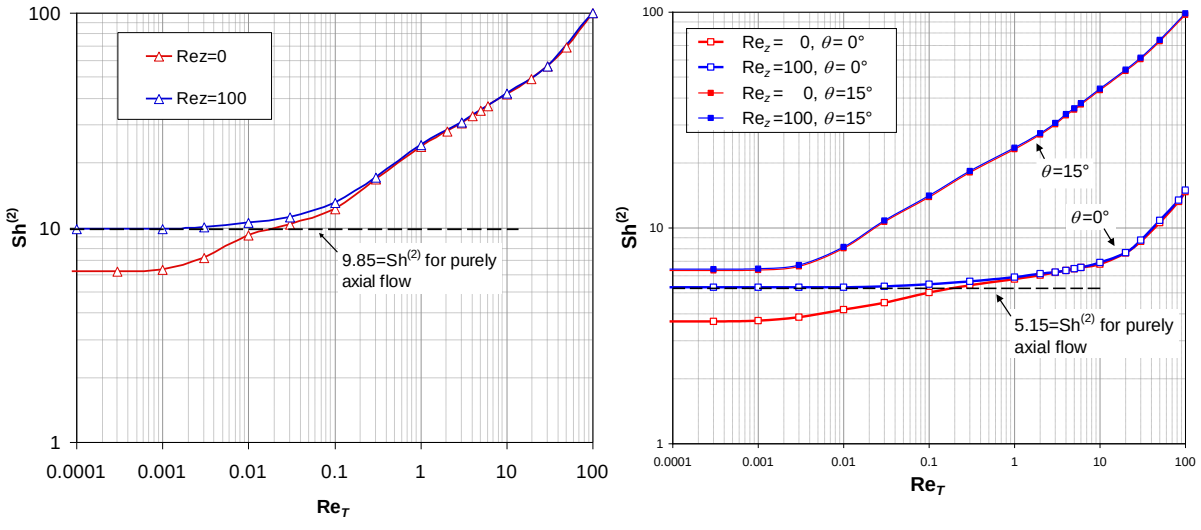

(a) (b)

Figure 16: Comparison of $Sh^{(2)}$ as a function of the transverse flow Reynolds number Re_T for different intensities of the axial flow. (a) hexagonal lattice with ε=0.5 and θ=10°; (b) square lattice with ε=0.5 and θ=0° or 15°.

In regard to mass transfer for mixed flow in a square lattice, the main difference is that the departure of the mixed-flow $Sh^{(2)}$ curve from the transverse-flow $Sh^{(2)}$ curve occurs only at those flow attack angles θ (practically, from 0° to 2-3°) at which, for $Re_T \to 0$, the value of $Sh^{(2)}$ in purely transverse

flow falls below that for purely axial flow ($Sh^{(2)}_{ax}\approx5.15$). At larger values of θ the transverse-flow $Sh^{(2)}$ remains larger than $Sh^{(2)}_{ax}$ at all Re_T and thus the mixed-flow $Sh^{(2)}$ coincides everywhere with its transverse-flow counterpart. **Figure 16(b)** documents this different behaviour for θ=0 and θ=15°. In summary, both for hexagonal and square lattices, in mixed flow the Sherwood number (in particular, $Sh^{(2)}$) is simply the larger between those computed for purely transverse flow at Re_T and for purely axial flow at Re_z.

4. Conclusions

High-accuracy finite volume numerical simulations were conducted for flow and mass transfer in regular square and hexagonal lattices of fiber bundles at low Reynolds number, ensuring steady-state conditions. Fully developed flow and concentration fields were assumed, the porosity ε was kept fixed at 0.5, and different combinations of axial and transverse flow (characterized by the respective Reynolds numbers Re_z, Re_T) were considered, letting also the flow attack angle θ in the cross-section plane vary.

A careful grid independence study was conducted and showed that finite volumes consisting of quadrilateral prisms are preferable to triangular prisms, since they allow a faster convergence of the results with the number of nodes, ensuring by far grid-independent results with ~10^5 finite volumes in the cross-sectional plane. In the axial direction just three volumes were used due to the fully-developed assumption.

In some cases, mean Sherwood numbers (dimensionless mass transfer coefficients) were computed for different wall boundary conditions, i.e. uniform wall mass flux (Neumann) or uniform wall concentration (Dirichlet). In the uniform mass flux case, it was shown that two different averages can be defined, based on circumferentially averaging either the local mass transfer coefficient ($Sh^{(1)}$) or the local wall concentration ($Sh^{(2)}$), and it was shown that the former suffers from an inconsistent definition and may take physically meaningless values. Therefore, the latter definition was used in most cases, and uniform wall mass flux conditions were preferred as closer to those expected in real fiber bundles with significant membrane resistance.

In purely axial flow ($Re_z\neq0$, $Re_T=0$), the Darcy friction coefficient f_z was found to vary strictly as $(Re_z)^{-1}$ in the whole range $Re_z\leq100$ investigated. The predicted Darcy hydraulic permeability, once expressed in dimensionless form, was in good agreement with literature results for the same porosity and was larger for the square lattice. The predicted Sherwood number was independent of Re_z, as expected in parallel flow, and was much larger for the hexagonal lattice.

In purely transverse flow ($Re_z=0$, $Re_T\neq0$), up to a transverse flow Reynolds number $Re_T\approx10$ the transverse Darcy friction coefficient f_T was found to be about the same at all flow attack angles θ and

to decrease almost exactly as $1/Re_T$. This shows that, at sufficiently low Reynolds numbers, the fiber lattice is hydraulically isotropic and the flow is self-similar. At higher Re_T, as the importance of inertial effects increases, f_T departs from the $(Re_T)^{-1}$ behaviour and develops a dependence from θ; at the highest Re_T investigated, it exhibits relative minima along the directions of symmetry (0°-30° for the hexagonal lattice, 0°-45° for thin good e square one) and maxima at intermediate directions. The predicted Darcy hydraulic permeability was in good agreement with literature results.

In regard to mass transfer, even limiting the discussion to $Sh^{(2)}$, the picture is quite complex. For $\theta \approx 0°$ $Sh^{(2)}$ remains low (<10) up to $Re_T \approx 10$ and then increases moderately. For other flow attack angles, $Sh^{(2)}$ starts increasing with Re_T already at very low values of this parameter ($\sim 10^{-3}$-10^{-2}), at different rates depending on θ. As a consequence, $Sh^{(2)}$ is low and flat with θ only at very low Re_T (<0.1), while for larger Re_T it exhibits relative minima along the directions of symmetry (0°-30°) and maxima at intermediate directions. Therefore, the lattice is hydraulically almost isotropic up to $Re_T \approx 10$, but is isotropic in regard to mass transfer only up to $Re_T \approx 0.1$. The anisotropy is more marked in the square lattice than in the hexagonal one, consistent with the lower degree of symmetry of the square arrangement.

In mixed flow ($Re_z \neq 0$, $Re_T \neq 0$), independent of the axial Reynolds number Re_z, the axial friction coefficient f_z remains unaffected by the transverse flow up to $Re_T \approx 10$ and then increases slightly with Re_T; in the whole range studied, the product $f_z Re_z$ (and thus the permeability K_z) is a function of Re_T only and not of Re_z nor of the Re_T/Re_z ratio. In its turn, the transverse friction coefficient f_T is unaffected by Re_z and thus is a function only of Re_T and θ. The Sherwood number (in particular, $Sh^{(2)}$) is simply the larger between those computed for purely transverse flow at Re_T and purely axial flow at Re_z.

Further studies will address irregular (random) fiber arrangements (more closely representative of real fiber bundles) and will use the friction and mass transfer correlations obtained by the present, small-scale, CFD analysis in the context of porous-media models of whole hollow fiber modules such as those used for haemodialysis.

Acknowledgments

Part of this work has been carried out with the financial support of the *Programma Operativo Nazionale Ricerca e Innovazione 2014-2020 (CCI 2014IT16M2OP005), Fondo Sociale Europeo, Azione I.1 "Dottorati Innovativi con caratterizzazione Industriale*".

Nomenclature

C	solute concentration [mol m^{-3}]
$\tilde{C}$	periodic component of solute concentration [mol m^{-3}]
C^*	dimensionless concentration [-]
C_{bulk}	bulk concentration [mol m^{-3}]
C_{LS}	large-scale component of concentration [mol m^{-3}]
C_{wall}	local concentration at the wall [mol m^{-3}]
D	diffusion coefficient of the solute [m^2 s^{-1}]
D_h	hydraulic diameter [m]
d	fiber diameter [m]
f_s	Darcy friction coefficient along the generic direction s [-]
f_T	Darcy friction coefficient along the cross-flow direction T [-]
f_z	Darcy friction coefficient along the axial direction z [-]
G_c	large-scale concentration gradient [mol m^{-4}]
G_p	large-scale pressure gradient [Pa m^{-1}]
J	local mass flux at the wall [mol m^{-2} s^{-1}]
K_s	hydraulic permeability [m^2]
k	Kozeny constant [-]
p	pressure [Pa]
$\tilde{p}$	periodic component of pressure [Pa]
p_{LS}	large-scale component of pressure [Pa]
Re_s	Reynolds number along a generic direction s [-]
Re_T	Reynolds number along the cross-flow direction T [-]
Re_z	Reynolds number along the axial direction z [-]
S	wet surface of the computational domain [m^2]
S_c	source term for the solute transport equation [mol m^{-3} s^{-1}]
$\mathrm{Sh}^{(1)}$	average Sherwood number for imposed wall mass flux according to definition 1 [-]
$\mathrm{Sh}^{(2)}$	average Sherwood number for imposed wall mass flux according to definition 2 [-]
$\mathrm{Sh}^{(CW)}$	average Sherwood number for imposed concentration at the wall [-]
s	generic direction [m]
T	cross-flow direction [m]
U	local shell-side mass transport coefficient [m s^{-1}]
$U^{(1)}$	average U according to definition 1 [m s^{-1}]
$U^{(2)}$	average U according to definition 2 [m s^{-1}]

$\vec{u}$	velocity vector [m s^{-1}]
$u_{s,sup}$	superficial velocity component along a generic direction *s* [m s^{-1}]
V	fluid volume [m^3]
V_{tot}	total volume, including shell and lumen [m^3]
x	Cartesian coordinate [m]
y	Cartesian coordinate [m]
z	Cartesian coordinate parallel to the fiber [m]

Greek symbols

ε	porosity [-]
θ	cross-flow attack angle (between *T* and *x*) [°]
μ	viscosity [Pa s]
ρ	density [kg m^{-3}]
Σ	specific surface of the medium particles [m^2]
$\vec{\sigma}$	unit vector along a generic direction *s* [m]

Averages

$\bar{\ }$	surface average
$\langle\ \rangle$	volume average

References

1. Sirkar KK. Membrane contactors. Adv Membr Technol Appl. 2008;685–702.
2. Yun CH, Prasad R, Guha AK, Sirkar KK. Hollow fiber solvent extraction removal of toxic heavy metals from aqueous waste streams. Ind Eng Chem Res. 1993;32:1186–95.
3. Al-Marzouqi MH, Marzouk SAM, Abdullatif N. High pressure removal of acid gases using hollow fiber membrane contactors: Further characterization and long-term operational stability. J Nat Gas Sci Eng. 2017;37:192–8.
4. Yang X, Yu H, Wang R, Fane AG. Optimization of microstructured hollow fiber design for membrane distillation applications using CFD modeling. J Memb Sci. 2012;421–422:258–70.
5. Scott K. Introduction to membrane separations. In: K. Scott, editor. Handbook of Industrial Membranes. Elsevier, Amsterdam; 1995. p. 3–185.
6. Vinther F, Jönsson AS. Modelling of optimal back-shock frequency in hollow fiber ultrafiltration membranes I: Computational fluid dynamics. J Memb Sci. 2016;506:137–43.

7. Zhang LZ, Li ZX, Zhong TS, Pei LX. Flow maldistribution and performance deteriorations in a cross flow hollow fiber membrane module for air humidification. J Memb Sci. 2013;427:1–9.
8. Kerr PG, Huang L. Review: Membranes for haemodialysis. Nephrology. 2010;15(4):381–5.
9. Eloot S, De Wachter D, Van Tricht I, Verdonck P. Computational flow modeling in hollow-fiber dialyzers. Artif Organs. 2002;26(7):590–9.
10. Taskin ME, Fraser KH, Zhang T, Griffith BP, Wu ZJ. Micro-scale modeling of flow and oxygen transfer in hollow-fiber membrane bundle. J Memb Sci. 2010;362(1–2):172–83.
11. Yang M-C, Cussler EL. Designing hollow-fiber contactors. AIChE J. 1986;32(11):1910–6.
12. Zhuang L, Guo H, Dai G, Xu Z liang. Effect of the inlet manifold on the performance of a hollow fiber membrane module-A CFD study. J Memb Sci. 2017;526:73–93.
13. Wickramasinghe SR, Semmens MJ, Cussler EL. Mass transfer in various hollow fiber geometries. J Memb Sci. 1992;69(3):235–50.
14. Costello MJ, Fane AG, Hogan PA, Schofield RW. The effect of shell side hydrodynamics on the performance of axial flow hollow fiber modules. J Memb Sci. 1993;80(1):1–11.
15. Skelland AHP. Diffusional mass transfer. Wiley, New York; 1975.
16. Lemanski J, Lipscomb GG. Effect of shell-side flows on hollow-fiber membrane device performance. AIChE J. 1995;41(10):2322-6.
17. Mavroudi M, Kaldis SP, Sakellaropoulos GP. A study of mass transfer resistance in membrane gas-liquid contacting processes. J Memb Sci. 2006;272:103–15.
18. Happel J. Viscous flow relative to arrays of cylinders. AIChE J. 1959;5(2):174–7.
19. Doshi MR, Gill WN, Kabadi VN. Optimal design of hollow fiber modules. AlChE J. 1977;23(5):1975–8.
20. Winograd Y, Toren M, Solan A. Reverse osmosis in shell and tubes. Desalination. 1974;14:173–87.
21. Gostoli C, Gatta A. Mass transfer in a hollow fiber dialyzer. J Memb Sci. 1980;6:133–48.
22. Noda I, Brown-West DG, Gryte CC. Effect of flow maldistribution on hollow fiber dialysis - experimental studies. J Memb Sci. 1979;5(C):209–25.
23. Carroll T, Booker NA. Axial features in the fouling of hollow-fiber membranes. J Memb Sci. 2000;168:203–12.
24. Zheng J, Xu Y, Xu Z. Flow distribution in a randomly packed hollow fiber membrane module. J Memb Sci. 2003;211:263–9.
25. Mat NC, Lou Y, Lipscomb GG. Hollow fiber membrane modules. Curr Opin Chem Eng. 2014;4:18–24.

871 26. Pak A, Mohammadi T, Hosseinalipour SM, Allahdini V. CFD modeling of porous membranes.
872 Desalination. 2008;282:482–8.
873 27. Zhuang L, Guo H, Wang P, Dai G. Study on the flux distribution in a dead-end outside-in
874 hollow fiber membrane module. J Memb Sci. 2015;495:372–83.
875 28. Yu H, Yang X, Wang R, Fane AG. Numerical simulation of heat and mass transfer in direct
876 membrane distillation in a hollow fiber module with laminar flow. J Memb Sci. 2011;384:107–
877 16.
878 29. Eloot S, Vierendeels J, Verdonck P. Optimisation of solute transport in dialysers using a three-
879 dimensional finite volume model. Comput Methods Biomech Biomed Engin. 2006;9(6):363–
880 70.
881 30. Dierickx PW, De Wachter DS, Verdonck PR. Two-dimensional finite element model for
882 oxygen transfer in cross-flow hollow fiber membrane artificial lungs. Int J Artif Organs.
883 2001;24(9):628–35.
884 31. Günther J, Schmitz P, Albasi C, Lafforgue C. A numerical approach to study the impact of
885 packing density on fluid flow distribution in hollow fiber module. J Memb Sci. 2010;348:277–
886 86.
887 32. Lim KB, Wang PC, An H, Yu SCM. Computational studies for the design parameters of hollow
888 fiber membrane modules. J Memb Sci. 2017;529:263–73.
889 33. Zhang J, Chen X, Ding J, Fraser KH, Taskin ME, Griffith BP, et al. Computational study of the
890 blood flow in three types of 3D hollow fiber membrane bundles. J Biomech Eng.
891 2013;135(12):1–12.
892 34. Buetehorn S, Volmering D, Vossenkaul K, Wintgens T, Wessling M, Melin T. CFD simulation
893 of single- and multi-phase flows through submerged membrane units with irregular fiber
894 arrangement. J Memb Sci. 2011;384:184–97.
895 35. Cai JJ, Hawboldt K, Abdi MA. Analysis of the effect of module design on gas absorption in
896 cross flow hollow membrane contactors via computational fluid dynamics (CFD) analysis. J
897 Memb Sci. 2016;520:415–24.
898 36. Ma C, Liu Y, Li F, Shen C, Huang M, Wang Z, et al. CFD simulations of fiber-fiber interaction
899 in a hollow fiber membrane bundle: Fiber distance and position matters. Sep Purif Technol.
900 2019;209:707–13.
901 37. Gurreri L, Tamburini A, Cipollina A, Micale G, Ciofalo M. CFD prediction of concentration
902 polarization phenomena in spacer-filled channels for reverse electrodialysis. J Memb Sci.
903 2014;468:133–48.

38. Battaglia G, Gurreri L, Airò Farulla G, Cipollina A, Pirrotta A, Micale G, Ciofalo M. Membrane deformation and its effects on flow and mass transfer in the electromembrane processes. Int J Mol Sci. 2019;20(8):11–5.
39. La Cerva M, Ciofalo M, Tamburini A, Cipollina A, Micale G. On some issues in the computational modelling of spacer-filled channels for membrane distillation. Desalination. 2017;411:101-11.
40. Green DW, Perry RH. Perry's chemical engineers' handbook. 8th ed. McGraw-Hill, editor. New York; 2008.
41. Klein E, Holland F, Lebeouf A, Donnaud A, Smith JK. Transport and mechanical properties of hemodialysis hollow fibers. J Memb Sci. 1976;1(C):371–96.
42. Sparrow EM, Loeffler AL. Longitudinal laminar flow between cylinders arranged in regular array. AIChE J. 1959;5(3):325–30.
43. Skartsis L, Khomami B, Kardos JL. Resin flow through fiber beds during composite manufacturing processes. Part II: Numerical and experimental studies of newtonian flow through ideal and actual fiber beds. Polym Eng Sci. 1992;32(4):231–9.
44. Larson RE, Higdon JJL. Microscopic flow near the surface of two-dimensional porous media. Part 1. Axial flow. J Fluid Mech. 1986;166:449–72.
45. Miyagi T. Viscous flow at low Reynolds numbers past an infinite row of equal circular cylinders. J Phys Soc Japan. 1958;13:493-6.
46. Yeom J, Agonafer DD, Han J-H, Shannon MA. Low Reynolds number flow across an array of cylindrical microposts in a microchannel and figure-of-merit analysis of micropost-filled microreactors. J Micromech Microeng. 2009;19:065025.
47. Ishimi K, Koroyasu S, Hikita H. Mass transfer in creeping flow past periodic arrays of cylinders. J Chem Eng Japan. 1987;20(5):492-98.
48. Sangani AS, Acrivos A. Slow flow past periodic arrays of cylinders with application to heat transfer. Int J Multiphase Flow. 1982;8(3):193-206.